Applied Chemical Engineering (2025) Volume 8 Issue 3 ISSN: 2578-2010 (O)
doi: 10.59429/ace.v8i3.5751

ORIGINAL RESEARCH ARTICLE

Synthesis, characterization, and redox-responsive novel molecular switching behavior of copper (II)–Viologen adduct complexes

Jinan. A. Azouz[1*], Wathiq. S. Abdul-Hassan[2]

[1*] *Ministry of Education, Directorate of Education Al-Muthanna, Al-Samawah, Al-Muthanna, 66001,Iraq*

[2] *Department of Chemistry, College of Science, University of Thi-Qar, Nassiria, 64001, Iraq*

***Corresponding author:** Jinan Ahmed Azouz; Jinanahmed223@gmail.com

ABSTRACT

This study presents the synthesis and characterization of copper (II) complexes incorporating viologen units, designed to function as redox-responsive molecular switches. The tetradentate N_2O_2 ligand (AN) was first coordinated with copper (II) to produce the CuAN complex, which subsequently underwent axial coordination with pyridine, mono-methylviologen ($C_1V^{+}\cdot PF_6^{-}$), and bis-viologen ($V_2^{2+}\cdot 2PF_6^{-}$), affording the corresponding adducts. A comprehensive set of analytical techniques, including FT-IR, UV-Vis absorption spectroscopy, XRD, TG analysis, mass spectrometry, and cyclic voltammetry, was employed to confirm their formation and investigate their structural and electronic properties. The spectroscopic results verified coordination through C=N and C–O groups, while XRD confirmed the crystalline nature of both the ligand and its complexes, with noticeable variations in d-spacing values due to axial ligation. UV-Vis spectra revealed distinct shifts in absorption bands, indicating enhanced electron delocalization and planarity upon coordination. Thermal analysis established differences in stability, with CuAN–$V_2^{2+}\cdot 2PF_6^{-}$ exhibiting the highest resistance to decomposition. Electrochemical studies further demonstrated the redox activity of the complexes, particularly the reversible π–dimerization of viologen radicals under chemical and electrochemical reduction. Overall, the obtained results highlight the potential of these copper–viologen adducts as promising candidates for molecular switches, responsive materials, and electrochemical devices.

Keywords: Bis(acetylacetone)ethylenediamine; pyridine; mono-methylviologen; Viologen adducts; Molecular switches; π–Dimerization; Redox-responsive materials; Cyclic voltammetry

ARTICLE INFO

Received: 24 August 2025
Accepted: 12 September 2025
Available online: 24 September 2025

Graphical Abstract

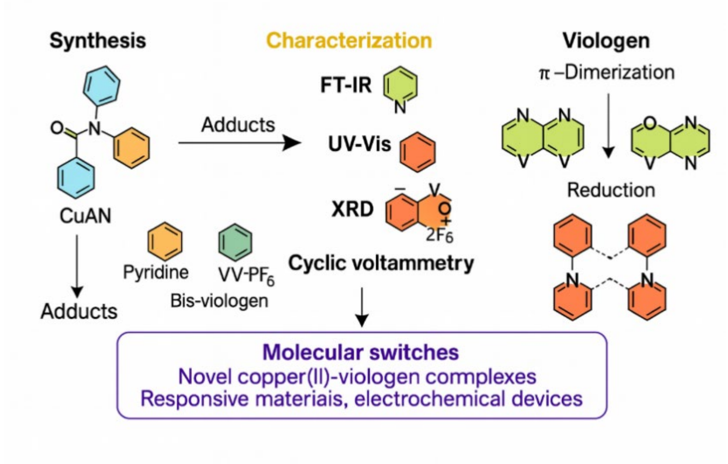

1. Introduction

Viologens are bipyridine organic salts in which one or both nitrogen atoms are quaternized. When both nitrogen atoms bear identical substituents, they are classified as 1,1′-disubstituted-4,4′-bipyridinium salts, whereas if the substituents differ, they are referred to as 1-substituent-1′-substituent′-4,4′-bipyridinium salts [1,2]. In the case where both substituents are methyl groups, the resulting dicationic species is known as methyl viologen. This compound was initially investigated as a redox indicator in biological research before later being identified as an effective herbicide. In 1933, Michaelis reported the violet coloration produced when 1,1′-dimethyl-4,4′-bipyridinium salt (DMV^{2+}) undergoes a one-electron reduction, forming a radical cation that stabilizes as a dimer (**Figure 1**). This phenomenon is widely recognized under the popular term “viologen” [3,4].

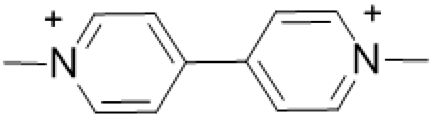

Figure 1. Dimethyl viologen

The main properties that make viologens important constituents in various materials include their ability to undergo sequential [5] and reversible reductions to yield reactive [6,7], intensely colored radical cations within experimentally accessible potentials [48-51]. **Figure 2** demonstrates the thermodynamic stability of the three redox states: the dication, the radical cation, and the neutral species [8-10].

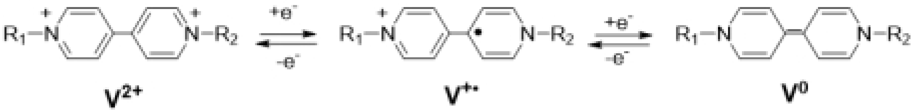

Figure 2. Three reversible redox states of viologen (V^{2+})

The objectives of this study were, first, the synthesis and characterization of a copper (II) complex with the tetradentate N_2O_2 ligand AN, affording the CuAN complex. Furthermore, the synthesis and characterization of adduct complexes were undertaken by axial coordination of CuAN with pyridine, $C1V^{+}\cdot PF_6^{-}$, and $V2^{2+}\cdot 2PF_6^{-}$ to yield CuANpy, $CuANC1V^{+}\cdot PF_6^{-}$, and $CuANV2^{2+}\cdot 2PF_6^{-}$, respectively. The aim was to develop novel electron-responsive copper (II) complexes utilizing π-dimerization of viologen radicals as the driving force for their switchable behavior. These switching processes can be induced either through chemical reduction, monitored by absorption spectroscopy, or through electrochemical reduction, examined by cyclic voltammetry in complexes containing viologen units. This study introduces a unique class of Cu (II)-viologen complexes with axial coordination and reversible π–dimerization, providing a new pathway for creating redox-responsive molecular switches.

2. Experimental part

2.1. Chemical reagents

All the chemical materials and solvents are of chemically source, and used without further purification.

2.2. Synthesis of CuAN complex

The CuAN complex (**Figure 3**) synthesized by dissolving AN (1 g, 4.458 mmol, 1 eq) in 3 mL of methanol, which was added dropwise over 10 minutes to solution of copper (II) acetate in 6 mL of a distilled water–methanol mixture (1:1) under continuous stirring. The reaction mixture was heated at 60 °C for 2 hours, and its progress was monitored by TLC using methanol/benzene (3:1) as the eluent. After completion, the mixture was cooled in an ice bath, affording a blue precipitate of CuAN complex. The solid product collected by filtration, washed thoroughly with cold distilled water, and dried to give 0.6 g (46.35%) with melting point of 260 °C [11,12].

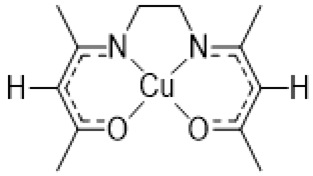

Figure 3. Chemical structure of CuAN complex formed by coordination of AN with copper (II) acetate

2.3. Synthesis of CuANPy complex

A solution of pyridine (2.85 mL, 2.77 g, 3.49 mmol, 20 eq) dissolved in a minimal amount of methanol was added dropwise with stirring to a solution of CuAN (0.5 g, 1.75 mmol, 1 eq) in 10 mL of methanol. The mixture was stirred at room temperature for 48 hours. The resulting precipitate was isolated by filtration, washed with methanol, and dried under vacuum to yield CuAN-py as a light blue solid (0.355 g, 55.62%). The product exhibited a melting point of 203 °C and was soluble in DMF. The molecular structure of the CuAN-py complex is illustrated in **Figure 3** [13,14].

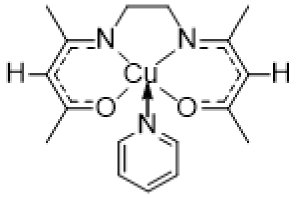

Figure 3. Chemical structure of the CuAN-py complex formed by the axial coordination of pyridine with the CuAN complex

2.4. Synthesis of CuAN-C1V+.PF6- complex

A solution of $C_1V^+\cdot PF_6^-$ (1 g, 3.35 mmol, 3 eq) in 10 mL of DMF was added with stirring to a solution of CuAN (0.31 g, 1.119 mmol, 1 eq) in 6 mL of DMF. The reaction mixture was stirred at room temperature for 30 days. The resulting precipitate was collected by filtration, washed with methanol, and dried under vacuum to yield CuAN–$C_1V^+\cdot PF_6^-$ as a dark brown solid (0.3 g, 46%, m.p. 246 °C). The complex is soluble in $CHCl_3$. The molecular structure of the CuAN–$C_1V^+\cdot PF_6^-$ complex is illustrated in **Figure 4** [5-7,15,16].

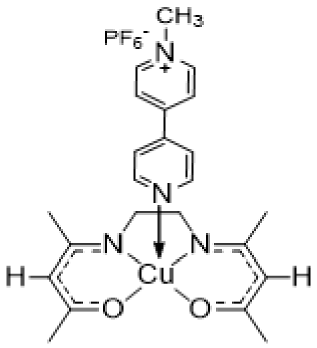

Figure 4. Chemical structure of the CuAN–$C_1V^+\cdot PF_6^-$ complex formed by axial coordination of mono-methyl viologen with CuAN

2.5. Synthesis of CuAN-V22+.2PF6- complex

A solution of $V_2^{2+}\cdot 2PF_6^-$ (1.4 g, 2.173 mmol, 2 eq) in 2 mL of DMF was added with stirring to a solution of CuAN (0.31 g, 1.085 mmol, 1 eq) in 3 mL of DMF. The reaction mixture was stirred at room temperature for 30 days. The resulting precipitate was collected by filtration, washed successively with methanol and MeCN, and then dried under vacuum to afford CuAN–$V_2^{2+}\cdot 2PF_6^-$ as a dark brown solid (0.5 g, 50%, m.p.

280 °C). The complex is soluble in DMF. The molecular structure of CuAN–$V_2^{2+}\cdot 2PF_6^-$ complex is shown in **Figure 5** [17].

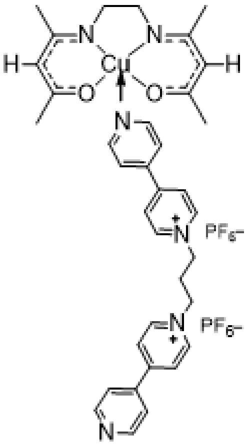

Figure 5. Chemical structure of the CuAN–$V_2^{2+}\cdot 2PF_6^-$ complex formed by axial coordination of bis-viologen with CuAN

3. Results and discussion

3.1. Mass spectrometry

The mass spectra of the CuANpy, CuAN–$C_1V^+\cdot PF_6^-$, and CuAN–$V_2^{2+}\cdot 2PF_6^-$ complexes exhibited characteristic peaks at m/z 870.47, 1185.10, and 1158.82, respectively, which correspond to fragments derived from the dimer of the molecular ion. A peak at m/z 583.60 was observed, indicating the loss of a CH_3 group from the molecular ion. In the case of CuAN–$C_1V^+\cdot PF_6^-$, a diagnostic peak at m/z 171 was assigned to the C_1V^+ fragment, as shown in Figure 2. For CuAN–$V_2^{2+}\cdot 2PF_6^-$, significant peaks were detected at m/z 352.95 and 157, corresponding to the V_2^{2+} and 4,4′-bipyridine moieties, respectively (**Figure 6-8**). In addition, other notable peaks were identified at m/z 860.47, 845.46, 791.39, 682.74, 505.54, 326.88, 243.75, and 184.85. Furthermore, peaks at m/z 1024.05, 761.40, 680.75, 816.10, 544.85, 503.60, 422.75, 243.85, and 185.85 were observed, along with peaks at m/z 1142.55, 855.15, 742.80, 636.95, 570.25, 284.20, 177.10, and 100 for CuANpy, CuAN–$C_1V^+\cdot PF_6^-$, and CuAN–$V_2^{2+}\cdot 2PF_6^-$, respectively. Fragment assignments, such as m/z 171 for C_1V^+, remain tentative as they lack MS/MS confirmation [11,18,19].

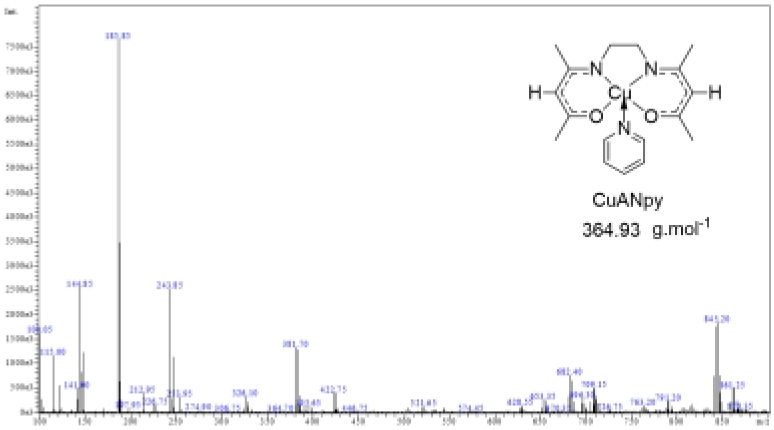

Figure 6. Electron impact LC- Mass spectrum of **CuAN-py**

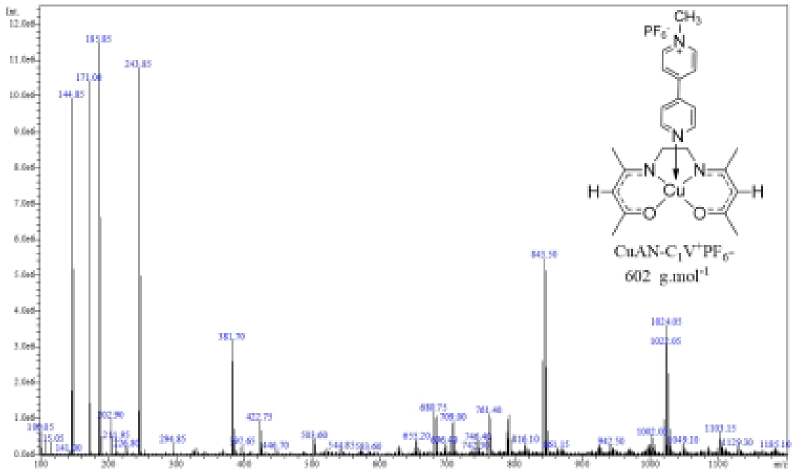

Figure 7. Electron impact LC-mass spectrum of CuAN-$C_1V^+.PF_6^-$

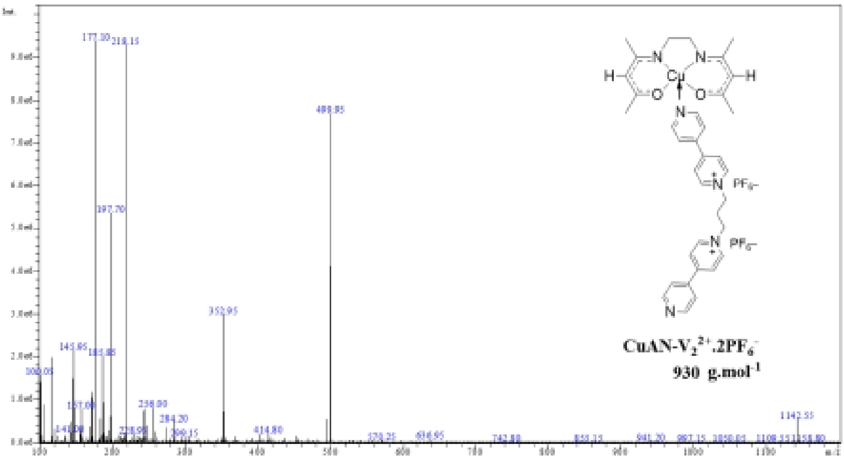

Figure 8. Electron impact LC-mass spectrum of CuAN-$V_2^{2+}.2PF_6^-$

3.2. FT-IR spectrometry of ligands and their Cu (II) complexes

FT-IR Spectra of the AN, CuAN and their adducts: CuANpy, CuANbpy, $CuANC_1V^+.PF_6^-$ and $CuANV_2^{2+}.2PF_6^-$ are recorded and depicted in **Figure 9.**

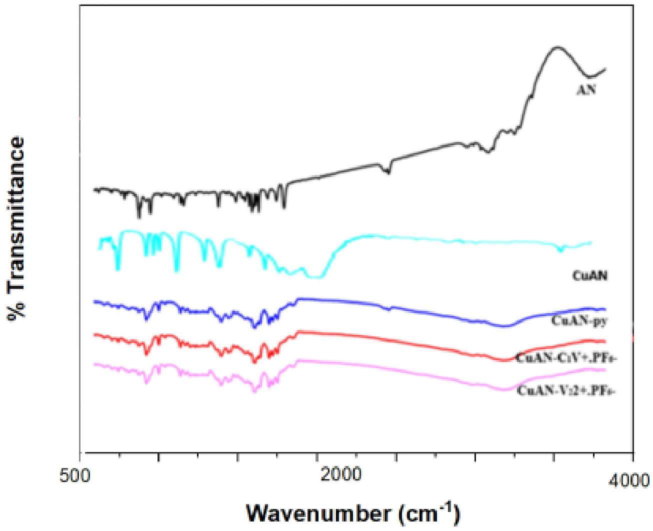

Figure 9. FT-IR spectra of AN, CuAN, CuANpy, $CuANC_1V^+.PF_6^-$ and $CuANV_2^{2+}.2PF_6^-$

The FT-IR spectra of AN showed bands at 3163 cm^{-1} which is attributed to stretching vibrations of hydrogen bonded OH [20,21]. While the band disappeared in copper (II) complexes: CuAN and their adducts: CuANpy, CuANbpy, CuAN-$C_1V^+.PF_6^-$ and CuAN-$V_2^{2+}.2PF_6^-$ which refer to deprotonation upon the complexation with Cu(II) metal ion. The OH bending vibrations of AN appeared at 1287 cm^{-1}. The bands at 3066 cm^{-1}, 3012 cm^{-1}, 3077 cm^{-1}, 3039 cm^{-1}, 3077 cm^{-1} and 3061 cm^{-1} occurred at AN, CuAN, CuANpy, CuANbpy, CuAN-$C_1V^+.PF_6^-$ and CuAN-$V_2^{2+}.2PF_6^-$ respectively are assigned to stretching vibrations of aromatic and/or olefinic C-H groups. While, the bending of these groups is noted at 739 cm^{-1}, 783 cm^{-1}, 782 cm^{-1}, 756 cm^{-1}, 782 cm^{-1} and 779 cm^{-1} respectively. The noted bands at 2999 cm^{-1}, 2920 cm^{-1}, 2998 cm^{-1}, 2912 cm^{-1}, 2995 cm^{-1} and 2995 cm^{-1} are assigned to stretching vibration of aliphatic C-H groups in AN, CuAN, CuANpy, CuANbpy, CuAN-$C_1V^+.PF_6^-$ and CuAN-$V_2^{2+}.2PF_6^-$. While, the bending of these groups is noted at 1371 cm^{-1}, 1354 cm^{-1}, 1355 cm^{-1}, 1396 cm^{-1}, 1355 cm^{-1} and 1357 cm^{-1} respectively [22,23]. The stretching vibrations of C=N groups in AN is noted at (1611, 1576) cm^{-1} These bands are blue shifted to be at 1577 cm^{-1}, 1578 cm^{-1}, 1585 cm^{-1}, 1578 cm^{-1} and 1645 cm^{-1} in CuAN, CuANpy, CuANbpy, CuAN-$C_1V^+.PF_6^-$ and CuAN-$V_2^{2+}.2PF_6^-$ respectively. The C=C [24,25] stretching vibrations happened at 1520 cm^{-1}, 1550 cm^{-1}, 1553 cm^{-1}, 1519 cm^{-1}, 1553 cm^{-1} and 1548 cm^{-1} in AN, CuAN, CuANpy, CuANbpy, CuAN-$C_1V^+.PF_6^-$ and CuAN-$V_2^{2+}.2PF_6^-$ respectively. The stretching vibration of C-O groups in AN appeared at 1287 cm^{-1}. At complexation, these bands are shifted to be at 1273 cm^{-1}, 1275 cm^{-1}, 1265 cm^{-1}, 1275 cm^{-1} and 1279 cm^{-1} in CuAN, CuANpy, CuANbpy, CuAN-$C_1V^+.PF_6^-$ and CuAN-$V_2^{2+}.2PF_6^-$ respectively [26,27]. The stretching vibrations of the coordination Cu-O bonds are seen at 455 cm^{-1}, 454 cm^{-1}, 424 cm^{-1}, 454 cm^{-1} and 468 cm^{-1} in CuAN, CuANpy, CuANbpy, CuAN-$C_1V^+.PF_6^-$ and CuAN-$V_2^{2+}.2PF_6^-$ respectively. The noted differences in the stretching vibrations among the ligands AN and their complexes: CuAN, CuANpy, CuANbpy, CuAN-$C_1V^+.PF_6^-$ and CuAN-$V_2^{2+}.2PF_6^-$ support well the complexation of Cu (II) metal ion with the groups C=N and C-O, i.e. formation of the coordination bonds Cu-NC and Cu-OC respectively.

3.3. X-ray diffraction of cupper (II) complexes

The XRD patterns of CuAN, CuANpy, CuANbpy, CuAN-$C_1V^+PF_6^-$ and CuAN-$V_2^{2+}.2PF_6^-$ are depicted in **Figures 10.**

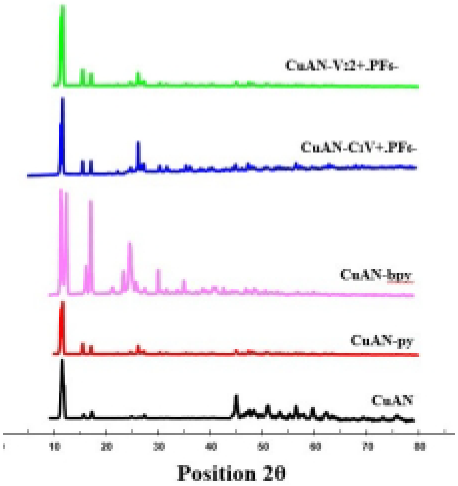

Figures 10. XRD patterns of CuAN, CuANpy, CuANbpy, CuAN-$C_1V^+PF_6^-$ and CuAN-$V_2^{2+}.2PF_6^-$.

The lattice strain is calculated by plotting β cosθ on the y-axis versus 4 sinθ on the x-axis where the slope represents the value of the lattice strain (**Figure 11** and **Table 1**). The intercept is equal to $k\lambda/D$. Therefore, the crystal size D is calculated from Eq (1) [28].

$$D=\frac{K\lambda}{\text{Intercept}} \tag{1}$$

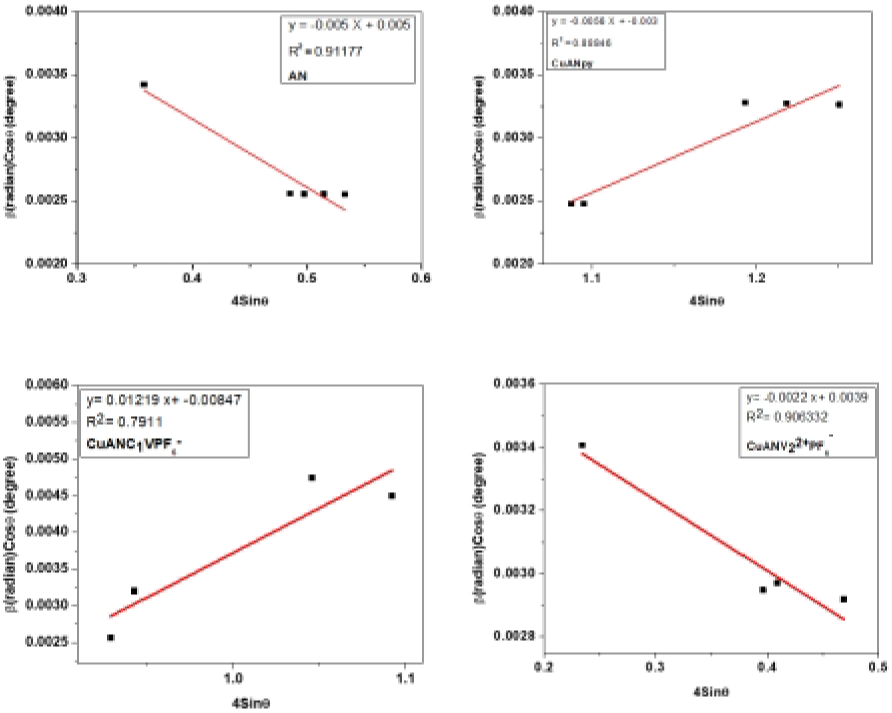

Figures 11. Williamson–Hall plot of the compound: AN and their Cu (II) Complexes

Table 1. Crystal size and strain of complexes from Scherrer and Williamson-Hall equations

Complexes	Crystal size Dp		Ɛ(Strain)
	Scherrer equation	**Williamson-Hall equation**	
AN	7.33	277.308	-0.005
CuAN	28.40	23.98	-6.2568×10^{-4}
CuANpy	7.2876	385.15	-0.0056
CuAN(bpy)	35	33.68	-1.03869×10^{-4}
CuAN-$C_1V^+PF_6^-$	9.008	163.700	0.01219
CuAN-$V_2^{2+}.2PF_6^-$	10.064	355.52	0.0022

First of all, the differences in peak numbers, intensities, D_p values support the formation of the CuAN from the ligand and confirm also the formation of the adduct complex from the precursor: CuAN. The XRD patterns are shown at angles $5° \leq 2\theta < 80°$. The largest peaks are observed at 25.2250° for AN, 11.76° for CuAN, 11.8250° for CuANpy, 11.46° for CuANbpy, 11.721° for CuANC$_1$V$^+$.PF$_6^-$ and 20.249° for CuANV$_2^{2+}$.2PF$_6^-$. It is noted the ligand AN is crystalline (XRD spectrum). After the complexation of AN, all AN complex (CuAN, CuANpy, CuANbpy, CuANC$_1$V$^+$.PF$_6^-$ and CuANV$_2^{2+}$.2PF$_6^-$) keep the crystalline nature. Among AN and these complexes, CuAV$_2^{2+}$.2PF$_6^-$ has the larger d-spacing (10.064) suggesting larger unit cell or lattice expansion. This expanded crystal structure is probably due to the larger structure among AN and these complexes. Also, the higher d-spacing for CuANC$_1$V$^+$.PF$_6^-$ (9.008) could be widely related to the larger PF$_6^-$ ion. Even if they have close values, the little lower d-spacing value of CuANpy (7.2876) than that of the free ligand AN (7.33) support that the complex has more planarity and restricted structure than spreaded ligand AN (see Uv-visible absorption spectroscopy item 3.5).

3.4. Thermal analysis of their Cu (II) complexes

The compounds CuAN and their Cu (II) Complexes Adducts were analyzed through TGA with a heating rate of 10°C/min in air atmosphere to predict the nature of volatile compounds produced while heating in the temperature range of 0 to 600°C [29]. The TG analysis curves of CuAN and their Cu (II) Complexes are depicted in **Figure 12.**

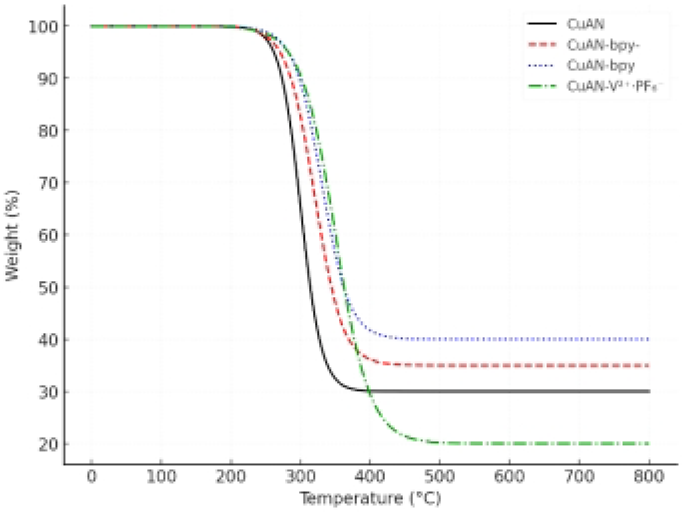

Figure 12. TGA of CuAN, CuANpy, CuANbpy and CuAN-$V_2^{2+}.2PF_6^-$.

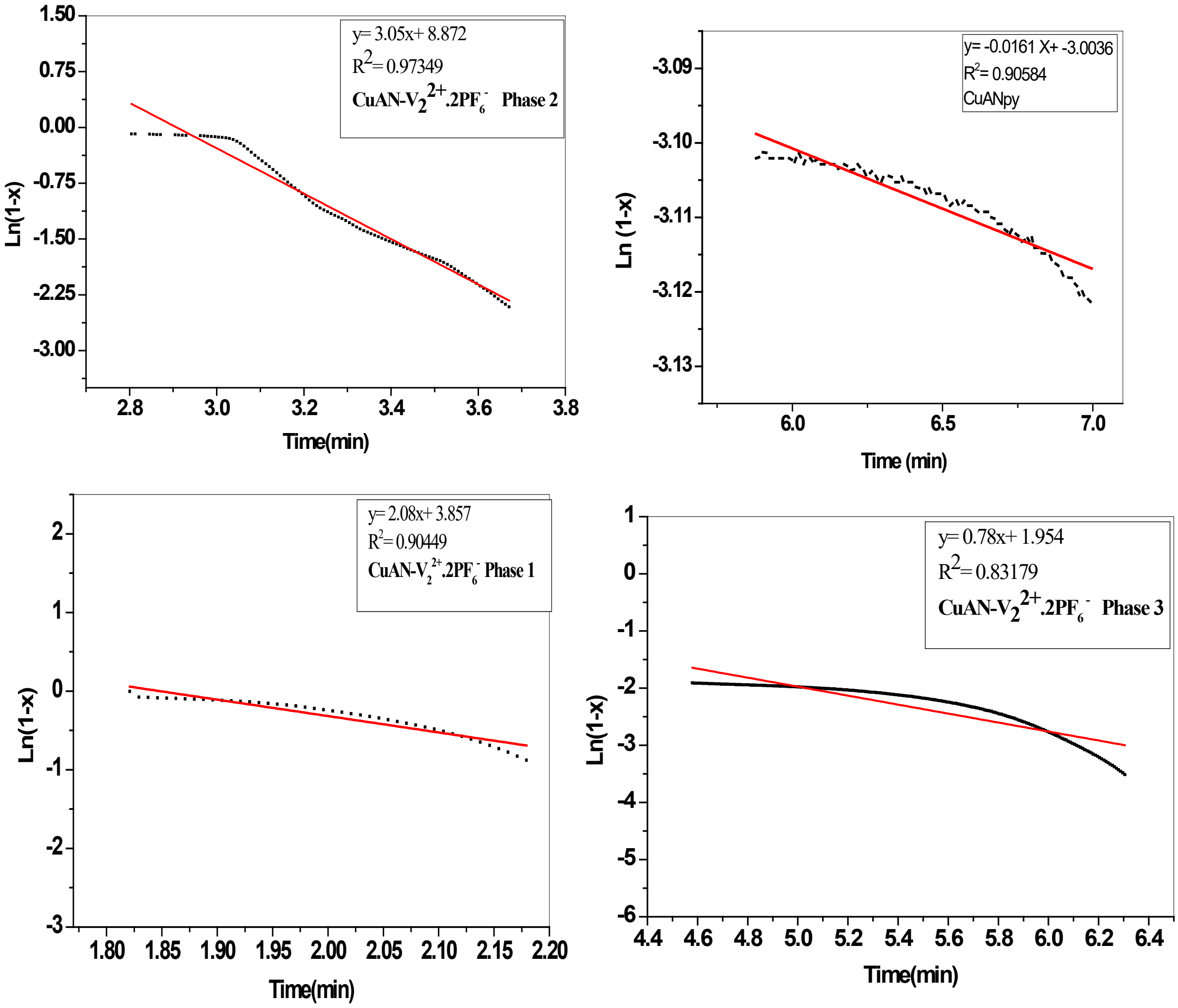

Figure 13. Plotts of ln (1- x) vs Time (min) of CuANpy and CuAN-$V_2^{2+}.2PF_6^-$ adducts.

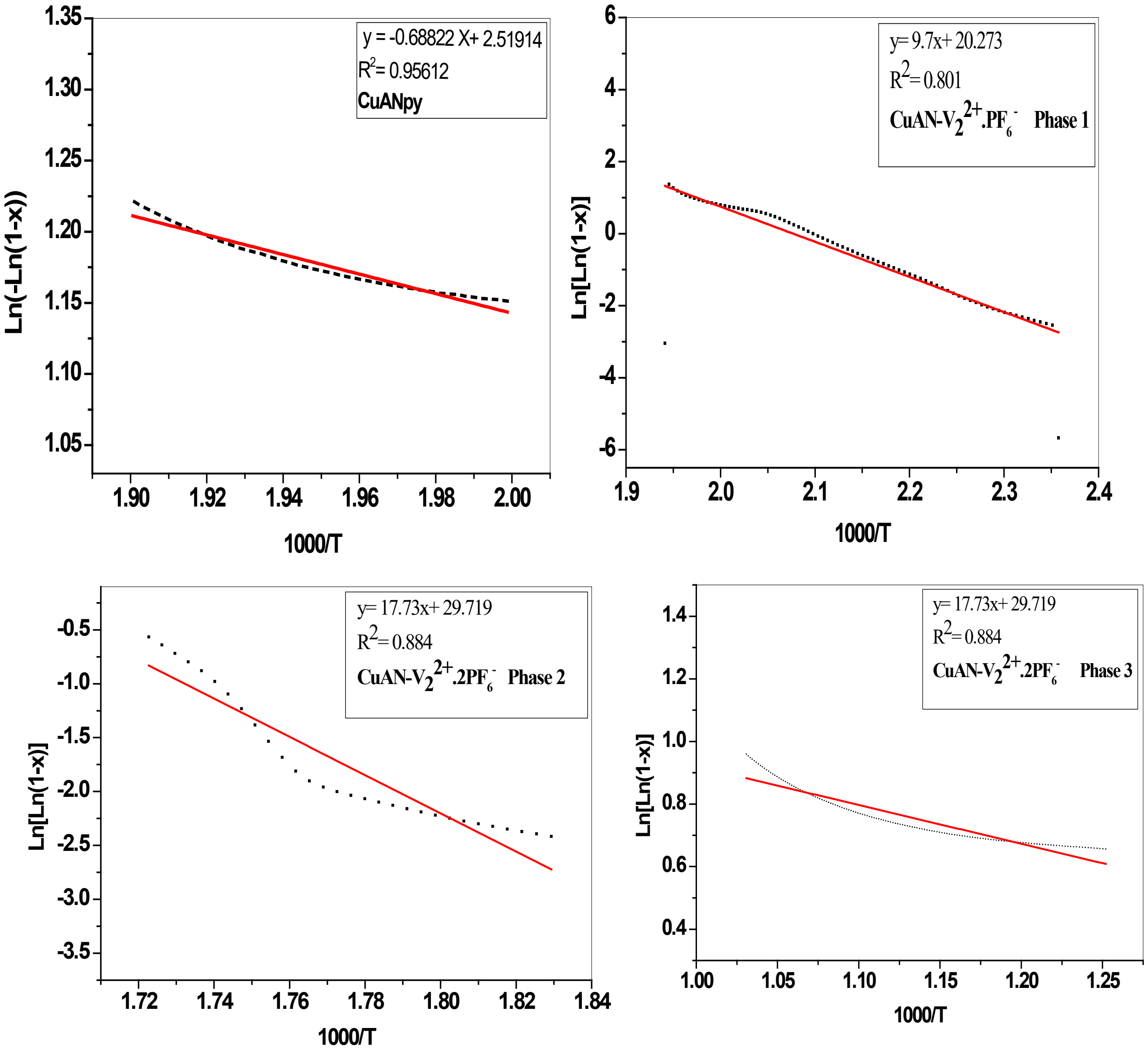

Figure 14. Plots of ln [-ln(1- x)] vs 1000/T of CuANpy and CuAN-V_2^{2+}.2PF_6^- adducts

Table 2. Kinetic and thermodynamic parameters of each phase during the thermogravimetric analysis of Copper (II) complexes (30)

Compounds	Phase No.	Temp. range (°C)	K (min^{-1})	t1/2 (min)	Ea (KJ·mol^{-1})	ΔH (KJ·mol^{-1})	ΔS (J mol^{-1} K^{-1})	ΔG (KJ·mol^{-1})
CuAN	1	166.76-272.36	64.9	0.01068	9507.651	4972.118	-280.789	158145.6
CuANpy	1	159.89-323.23	16.1	0.04304	5722.068	763.5853	-296.572	177632.9
CuANbpy	1	105.89 – 358.83	1146.38	0.00061	20700.28	15445.81	-255.656	177015.6
CuANV$_2^{2+}$.2PF$_6^-$	1	151-242	2.08	0.333	17.293	-3518.19	-175.78	70946
	2	252-373	3.05	0.227	25.35	-4218.84	-97.67	47073.5
	3	294- 806	0.78	0.888	6.485	-4705.16	-350.86	194284.9

The thermal decomposition of CuAN, CuANpy, and CuANbpy occurs in a single step, whereas CuAN–V_2^{2+}·2PF_6^- undergoes three decomposition steps (**Figure 13** and **14**). The decomposition processes were initiated at 105.89 °C, 151 °C, 159.89 °C, and 166.76 °C for CuANbpy, CuAN–$V_2^{2+}\cdot 2PF_6^-$, CuANpy, and CuAN, respectively. Beyond the final decomposition temperatures (T_{final} = 272.36–806.6 °C), all copper complexes were almost completely degraded. According to the International Confederation for Thermal Analysis and Calorimetry (ICTAC), a higher activation energy (E_a) within a series corresponds to greater thermal stability, and the opposite holds true. Based on the calculated E_a values presented in **Table 2,** the thermal stability follows the order:

$$\text{CuANpy} < \text{CuAN} < \text{CuANbpy} < \text{CuAN–}V_2^{2+}\cdot 2PF_6^-.$$

The axial coordination of pyridine to the copper (II) ion in CuAN is proposed to disturb the charge distribution within the five-coordinate complex (CuANpy), thereby decreasing its thermal stability, as reflected by its relatively low activation energy (E_a = 5722.07 × 10^3 J·mol^{-1}). In contrast, the enhanced charge distribution in CuANbpy accounts for its higher thermal stability (E_a = 20700.28 × 10^3 J·mol^{-1}). Furthermore, the axial coordination of $V_2^{2+}\cdot 2PF_6^-$ to the Cu(II) ion in CuAN is suggested to induce the formation of a saddle-shaped complex, CuAN–$V_2^{2+}\cdot 2PF_6^-$, exhibiting the highest thermal stability among the studied complexes.

3.5. UV-Visible absorption spectroscopy of ligand and their Cu (II)-complexes

UV-Visible absorption spectra of the ligands AN and their Copper (II) complexes were recorded in different solvents ($CHCl_3$, DCM, Acetone, EtOAc, MeCN, EtOH, MeOH, DMF and DMSO). These spectra were recorded at low and high Concentrations. The absorption spectra of low and high Concentrations were performed to note clearly UV and Visible absorption bands respectively of copper (II) complexes. The absorption spectra are depicted in **Figures 10-20**. these complexes are listed in **Table 3, Figures 15** and **16** represent electronic absorption spectra of CuAN and copper (II) acetate in DMF.

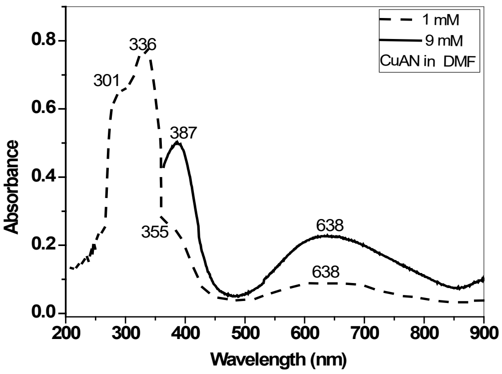

Figure 15. UV-Visible absorption spectra of 9 mM (black solid line) and 0.07 mM (black dash line) of **CuAN** in DMF at r.t using quartz cell with path length of 1 cm.

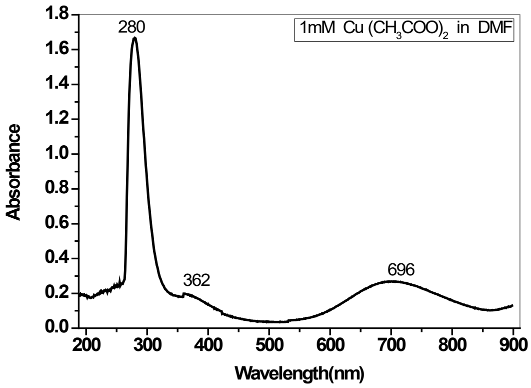

Figure 16. UV-Visible absorption spectrum of 1mM (Black Solid line) $Cu(CH_3COO)_2$ in DMF r.t using quartz cell with a path length of 1cm.

The d-d transition bands of CuAN and copper acetate in DMF occurred at 638 nm and 696 nm respectively [31,32]. The d-d transition bands of CuAN are shifted to shorter wavelengths by 58 nm Compared to that of copper (II) acetate. These two shifts reflect that the complexation happened among Cu^{2+} ion and both of AN. UV absorption bands occurred at 301 nm for CuAN is also red shifted Compared to that of copper (II) acetate happened at 280 nm. which reflect easier UV. absorption transition in complexes. The complex CuAN absorbs also at 336 nm and 355 nm. Also, CuAN complex in DCM and DMSO solvent showed in **Figures 17** and **18.**

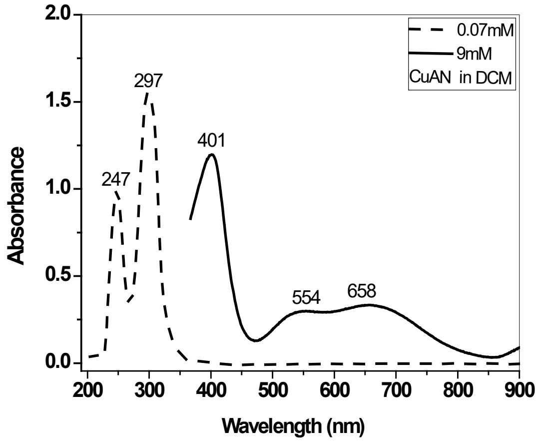

Figure 17. UV-Visible absorption spectra of 9 mM (black solid line) and 0.07 mM (black dash line) of CuAN in DCM at r.t using quartz cell with path length of 1 cm.

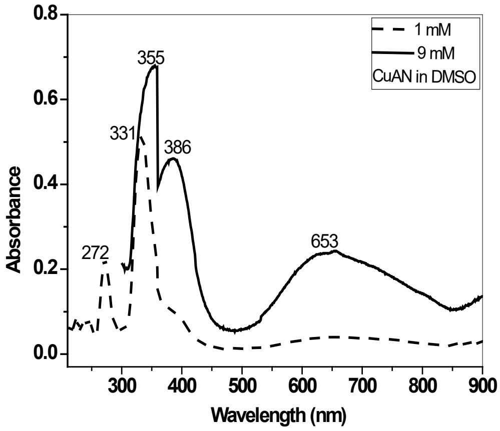

Figure 18. UV-Visible absorption spectra of 0.008 mM of CuAN in DMSO at r.t using quartz cell with path length of 1 cm.

The ligand AN absorbs at 233 nm, 305 nm, 322 nm in MeOH and at 315 nm in DMF and at 318 nm in DMSO See **Figures 19** and **20.**

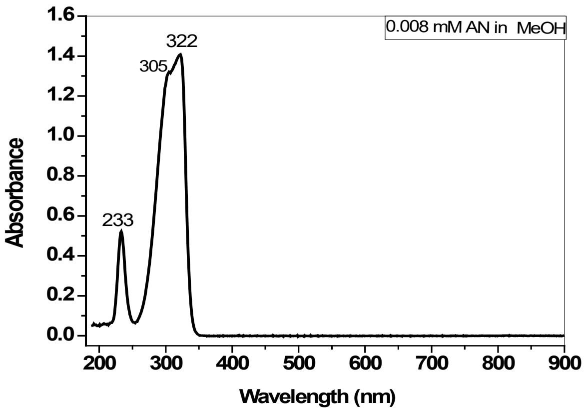

Figure 19. UV-Visible absorption spectrum of 0.008mM of AN in MeOH at r.t using quartz cell with path length of 1 cm.

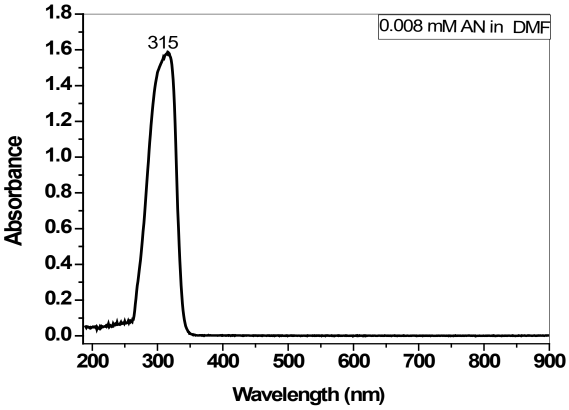

Figure 20. UV-Visible absorption spectrum of 0.008mM of AN in DMF at r.t using quartz cell with path length of 1 cm.

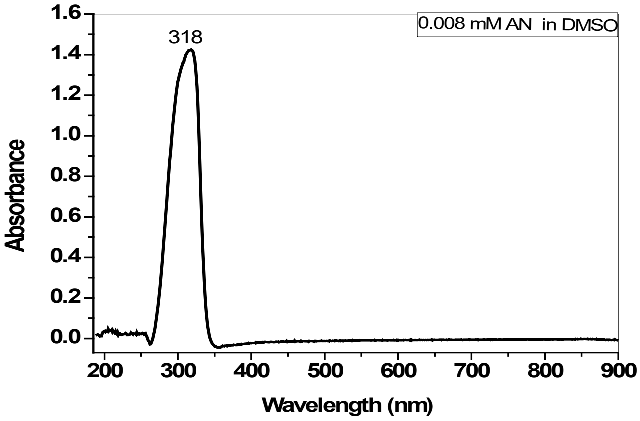

Figure 21. UV-Visible absorption spectrum of 0.008mM of AN in DMSO at r.t using quartz cell with path length of 1 cm.

Table 3. Maximum wavelengths and molar absorption coefficients for AN and its CuAN, CuANpy, CuANbpy, $CuANC_1V^+.PF_6^-$ and $CuANV_2^{2+}.2PF_6^-$ in different solvents.

Compounds	Concentration (mM)	λ max/ nm (Ɛ. $M^{-1}.cm^{-1}$)	Solvent
CuANpy	10	414(163.4), 530 (65.7), 657(79.9)	$CHCl_3$
	0.0045	251(146666.67), 299(271555.56)	
CuAN	9	401 (137.9), 554 (29.12), 658 (31.12)	DCM
	0.07	247 (14258.57), 297 (22287)	
$CuANC_1V^+.PF_6^-$	1	385 (801.1), 510 (190.2) , 680 (200.1)	
	0.02	249 (39510), 299 (67550)	
$CuANV_2^{2+}.2PF_6^-$	3	423(304.1)	MeCN
	0.02	291(78355)	
AN	0.008	233(65262), 305(163750), 322(176875)	MeOH
	0.008	315 (198000)	DMF
CuAN	1	301 (655), 336 (778), 355 (271), 638 (91)	
	9	387 (55.778), 638 (25.44)	
CuANpy	10	407 (182.3), 636 (119.9)	
	0.03	296 (45166.67)	
CuANbpy	10	399 (17.55), 624 (11.59)	
	0.06	294 (16.87)	
$CuANV_2^{2+}.2PF_6^-$	3	423 (277.37)	
	0.1	286 (15531)	
AN	0.008	318 (177875)	DMSO
CuAN	1	272 (223), 331 (510)	
	9	355 (75.556), 386 (51.22), 653(27)	
CuANbpy	10	397 (157.9), 632 (92.1)	
	0.06	298 (18.78)	
$CuANV_2^{2+}.2PF_6^-$	3	423 (307)	
	0.06	298 (25533.33)	

The absorption behavior of AN (**Figure 21** and **Table 3**) is oscillatory with increasing solvent polarity. In other words, both electronic transitions approach each other as solvent polarity increases. For the ligand AN, intermolecular hydrogen bonding occurs between the C=N and O–H groups (C=N···OH). This is supported by its presence as a 100% hydrogen-bonded structure in DMSO-d_6, although the extent of hydrogen bonding decreases with increasing solvent polarity [33]. Such hydrogen bonding weakens the n–π* transition, causing a blue shift. Consequently, along with the previously mentioned factors, the strong hydrogen bonding in this ligand brings the n–π* transition closer to the π–π* transition. As a result, the more intense π–π* transition overlaps with the weaker n–π* transition in AN. Upon complexation with Cu^{2+} ions, the characteristic twisted geometry of the free AN ligand is converted into the planar structure of the CuAN complex. This increased planarity enhances electron delocalization in the coordinated ligand compared with the free ligand, resulting in red shifts in its absorption bands. Accordingly, the ligand absorptions in CuAN (301, 336, and 355 nm in DMF; 272, 331, and 355 nm in DMSO) are red-shifted relative to those of the free AN ligand (315 nm in DMF and 318 nm in DMSO) (**Figures 22, 23, 24** and **25**). Overall, the differences in the positions and intensities of the UV absorption bands between the copper (II) complexes and their free ligands confirm the formation of copper (II) complexes with greater planarity than the corresponding ligands. In the visible region, the absorption bands arise from electronic transitions between split d-orbital energy levels. For CuAN, two distinct bands were observed in various solvents: a sharp high-energy band and a broad low-energy band, both attributable to d–d transitions of coordinated Cu (II) ion. Specifically, intense bands were recorded at 401 nm, 387 nm, and 386 nm in DCM, DMF, and DMSO, respectively, which are assigned to the electronic transition d_{xz}, d_$_{yz}$ → d_{xy}. Notably, in DCM two well-resolved bands were identified, corresponding to the $d_{x^2-y^2}$ → d_{xy} and d_{z^2} → d_{xy} transitions. In DMF and DMSO, these transitions merged to appear as a single broad band centered at 638 nm. Furthermore, the reactions of CuAN with pyridine, bpy, $C_1V^{+}\cdot PF_6^{-}$, and $V_2^{2+}\cdot 2PF_6^{-}$ at room temperature afforded the corresponding adducts, each exhibiting distinct TLC profiles (different spots), solubilities, colors, and melting points [34,35].

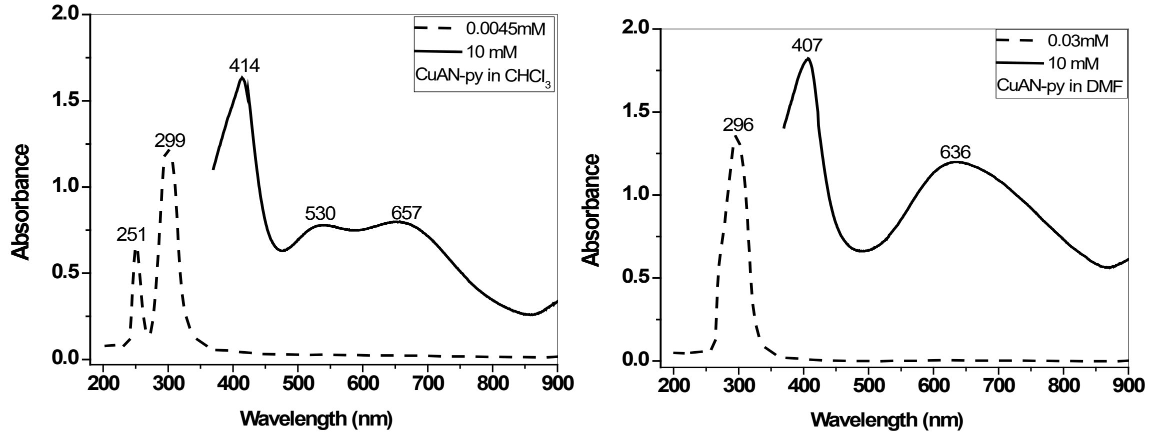

Figure 22. UV-Visible absorption spectra of 10 mM (black solid line) and 0.0045mM, 0.03 mM (black dash line) of CuAN-bpy in DMF and DMSO at r.t using quartz cell with path length of 1 cm

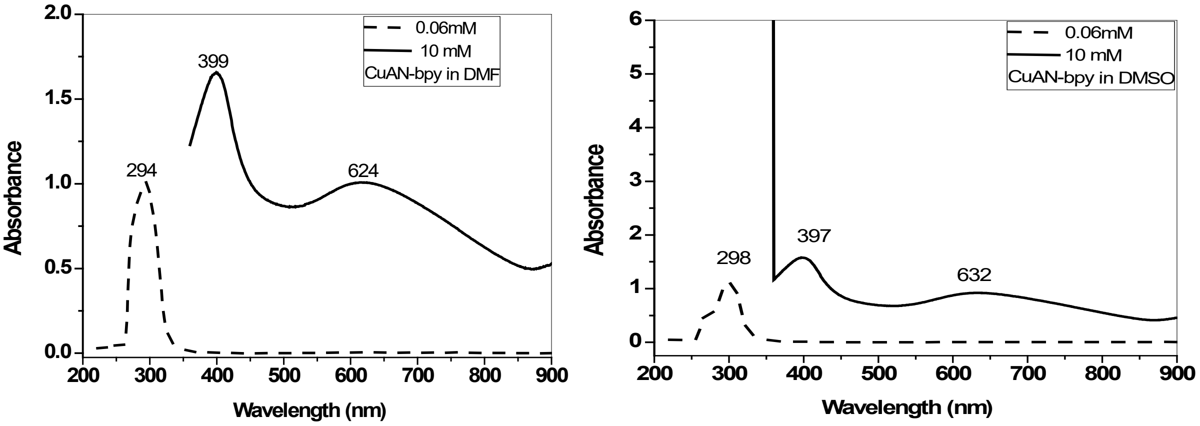

Figure 23. UV-Visible absorption spectra of 10 mM (black solid line) and 0.06 mM (black dash line) of CuAN-bpy in DMF and DMSO at r.t using quartz cell with path length of 1 cm.

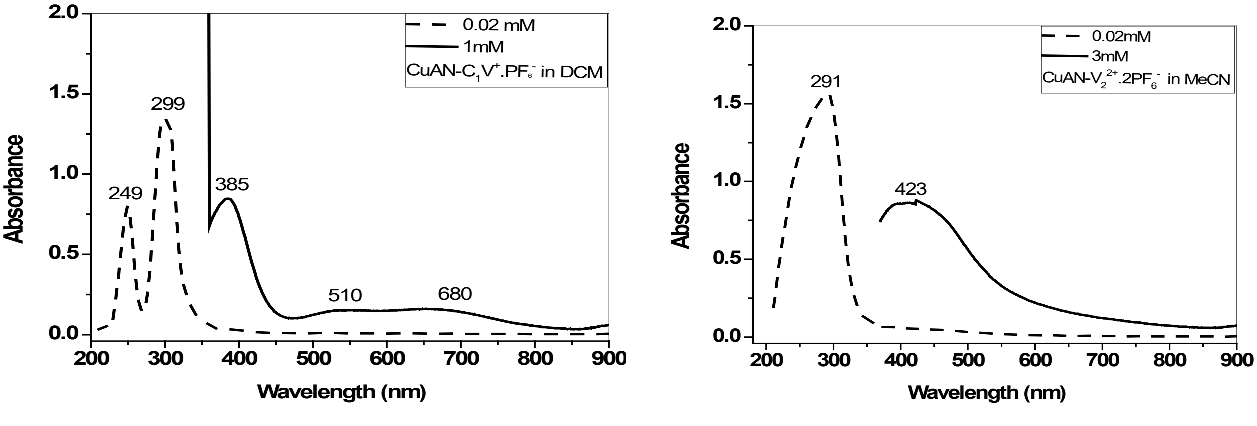

Figure 24. UV-Visible absorption spectra of 1 mM, 3mM (black solid line) and 0.02 mM (black dash line) of CuAN-$C_1V^{+}.PF_6^{-}$ in DCM and MeCN respectively at r.t using quartz cell with path length of 1 cm.

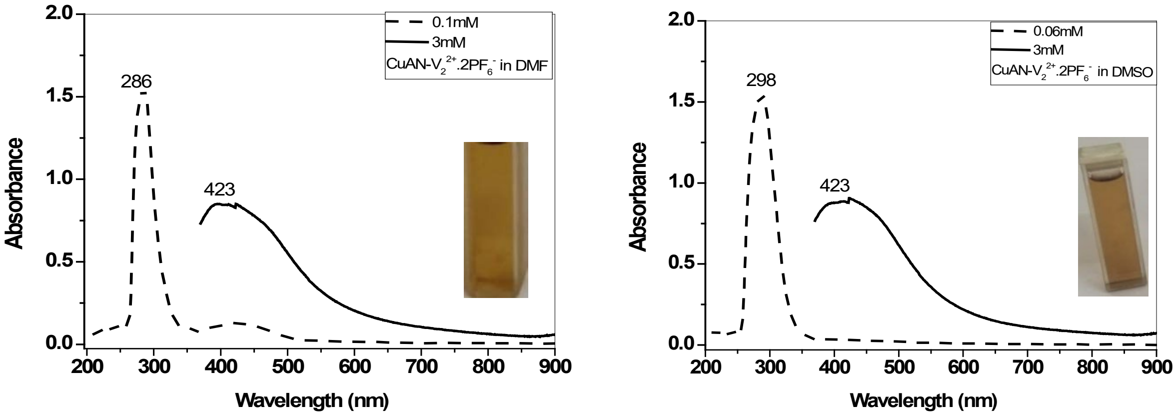

Figure 25. UV-Visible absorption spectra of 3 mM (black solid line) and 0.1mM, 0.06 mM (black dash line) of CuAN-V_2^{2+}.2PF_6^- in DMF and DMSO respectively at r.t using quartz cell with path length of 1 cm.

These resulted adducts have notable different physical properties compared with the precursor Complex CuAN like their TLC behavior, Solubilities, Colors and melting points Similarly, to less extent, the case with CuAN adducts. It was noted that uv absorptions of CuAN Adducts in DMF are blue shifted with those of the precursor Complex CuAN. This blue shift reflects the hardy uv transitions to happen in CuAN adducts compared with those of CuAN. Also, bluer shift was noted for the adduct that have positive ligand: CuANV_2^{2+}.2PF_6^- Compared with the adducts of py and bpy: CuANpy and CuANbpy respectively [36]. UV transitions in CuAN adducts are red shifted at increasing the polarity of Solvent. This note refers to increase of the property of the π-π* transition in UV absorptions bands that are assigned before to π-π* transition merged with n-π* in the precursor Complex: CuAN. Therefore, while CuAN absorbs at 301 mm in DMF, its adduct: CuANpy, CuANbpy and CuANV_2^{2+}.2PF_6^- absorb at 296 mm, 294 nm and 286 mm respectively. As mentioned before, the d-orbital energy distribution of Squar planer geometries of CuAN decrease in the order dxz, dyz < dz² < dx²-y² < dxy. After axial interaction of CuAN with py, bpy, C_1V^+.PF_6^- , V_2^{2+}.2PF_6^- and drawing on the results of X-ray Crystal Structures published before, the most favored arrangement for S: Coordinate Copper (II) in β-diketone compounds is the Square pyramidal structure. The d-orbital energy levels for the Square pyramidal 1:1 adduct of CuAN decrease in the order = dxz, dyz < dx²-y² < dz² < dxy. This splitting patters produces three d-d transition bands resolution Referring to the crystal field splitting for S: coordinate Square pyramidal Copper (II), an increase in δ interaction along the 2 axis is directed primarily at the dz² orbital. The effect of the raising the energy of this is to decrease the dz²→dxy transition energy producing a shift in the spectrum to lower frequencies compared with the Complex of square planar geometry of the precursor Complexe (CuAN). Based an the above interpretations, the d-d transitions of CuANpy and CuANC_1V^+.PF_6^- occurred at 414 nm, 530 nm, 657 nm in $CHCl_3$ and at 385 nm, 510 nm, 680 nm respectively [37]. Consequently, these three d-d transition bands Could be assigned to dxz, dyz → dxy, dx²⁻y² → dxy and dz² → dxy respectively. It is clearly noted that the transition dz² → dxy in the square pyramidal Complex CuANC_1V^+.PF_6^- (680 nm) is easier to happen compared with that transition(658 nm) occurred in the Square planer precursor Complex. CuAN in the solvent: DCM. The other adduct complexes CuANpy in DMF and CuANbpy showed two d-d transition bands. Here, the Second broad band could be an attributed as merged two transitions which are dx²⁻y²→ dxy and dz² → dxy.

3.6. Electrochemical studies

The electrochemical properties of the N_2O_2 ligand AN, β-diketone ligand A, their complexes and adducts along with the references Compounds: $Cu(OAC)_2$, bpy, C_1V^+.PF_6^- and V_2^{2+}.2PF_6^- have been investigated in DMF +0.1M [38]. TBAP using cyclic Voltammetry (CV) (**Figure 26** and **27, Table 4**). All the potentials in the text are given against Ag pseudo reference electrode. In order to avoid a chemical oxidation of the electro generated compounds under air, all electrochemical experiments have been carried out at room temperature under an argon atmosphere using a Conventional three electrode electrochemical cell. A vitreous Carbon disc electrode was used as working electrode and a platinum wire as auxiliary electrode. The half-wave potentials are systematically tabulated for clarity, which helps distinguish between Cu^{2+}/Cu^{+} and viologen-centered reductions.

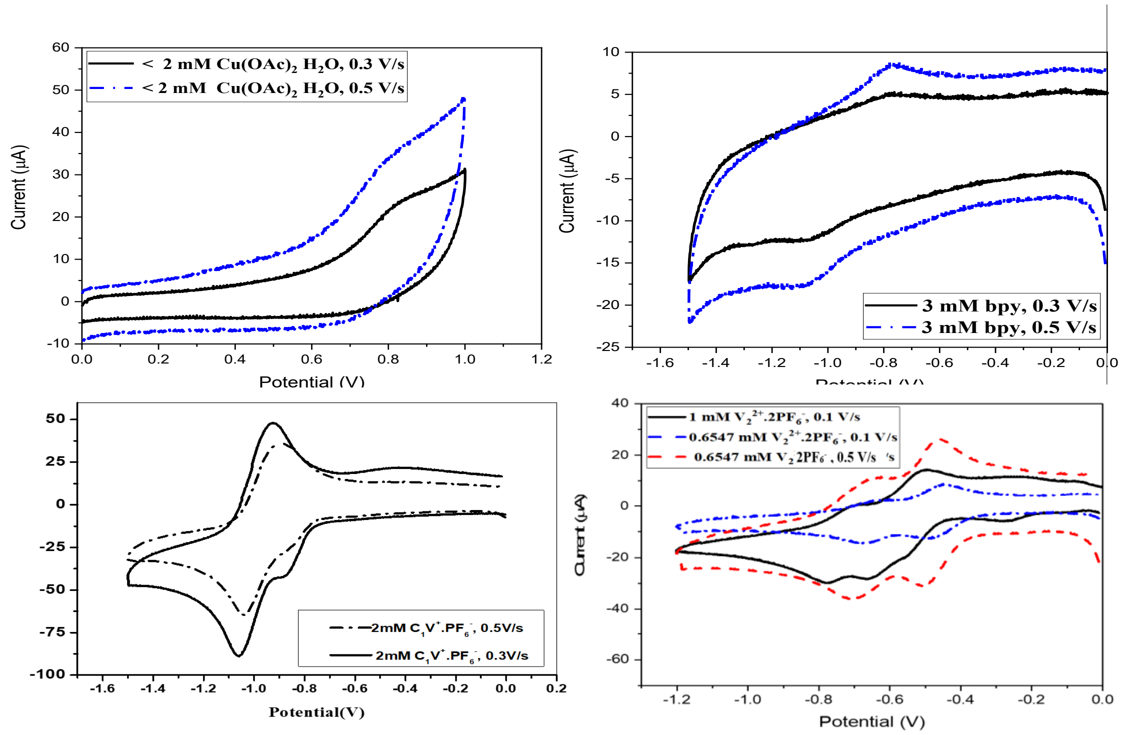

Figure 26. CVs of $Cu(OAC)_2$, $C_1V^{+}.PF_6^{-}$, bpy, $V_2^{2+}.2PF_6^{-}$ in 0.1M TBAP/DMF of Working electrode: 3 mm Vitreous Carbon. Reference electrode: Ag quasi- reference electrode.

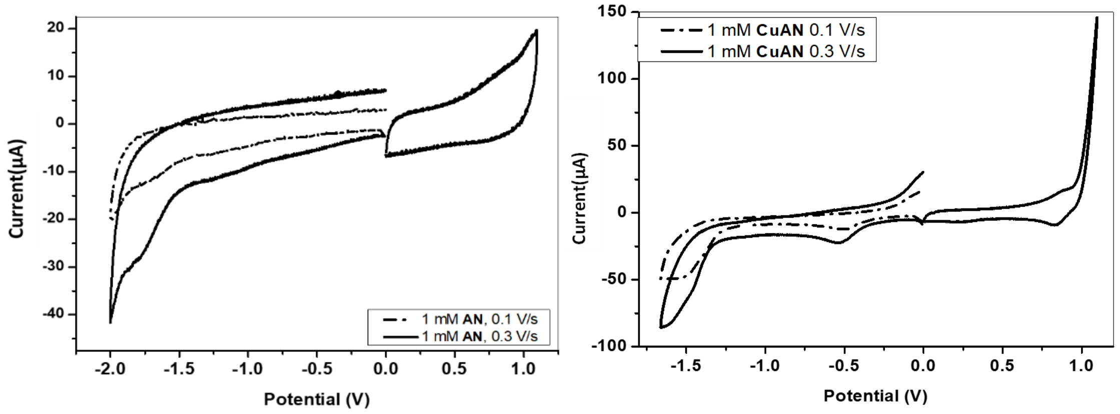

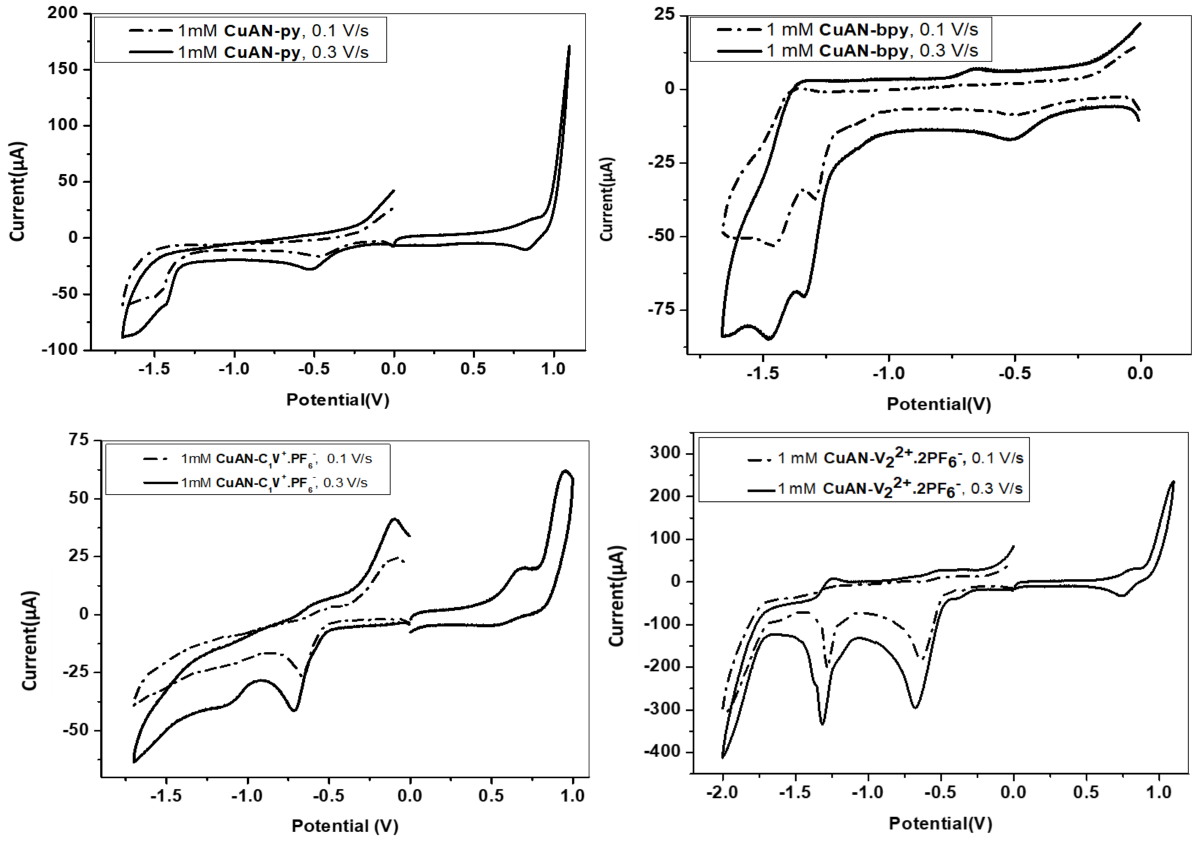

Figure 27. CVs of AN, CuAN, CuANpy, CuANbpy, CuANC$_1$V$^+$.PF$_6^-$ in 0.1M TBAP/DMF of Working electrode: 3 mm Vitreous Carbon. Reference electrode: Ag quasi- reference electrode.

Table 4. Experimental voltametric potentials with number of transferred electrons (in parenthesis) for the compound AN and their Cu(II) Complexes Adduct at 0.1 mV/s. Working electrode: 3mm Vitreous Carbon. Reference electrode: 0.1 M TBAP/DMF.

Compound	Conc. (mM)	(V/s)	Epc (mV)	Ipc (µA)	Epa (mV)	Ipa (µA)	ΔE (mV)	E$_{1/2}$ (mV)	$^{ipa}/_{ipc}$
Cu(OAc)$_2$	< 2	0.3	-	-	845.666	19.869	-	-	-
		0.5	-	-	938.291	24.953	-	-	-
bpy	3	0.3	-1092	-4.423	-766.229	1.168	325.771	-929.1145	0.2640
		0.5	-1113	-6.686	-766.535	4.412	346.465	-939.7675	0.6598
C$_1$V$^+$.PF$_6^-$	2	0.3	-930.393	-26.765	-	-	-	-	-
			-1.038	-34.65	-902.56	36.068	-901.522	-451.799	-1.041
		0.5	-	-	-	-	-	-	-
V$_2^{2+}$. 2PF$_6^-$	0.6547	0.1	-504.915	-10.123	-436.979	7.101	67.936	-470.947	0.7014
			-690.779	-3.6	-612,109	5.807	39.335	-651.44	1.6130
		0.5	-515.956	-21.163	-422.564	-21.163	93.392	-469.26	0.7291
			-715.009	-9.191	-613.105	16.644	101.904	-664.05	1.8109
AN	1	0.1	-1747	-5.727	-	-	-	-	-
		0.3	-1809	-14.802	-	-	-	-	-
CuAN	1	0.1	-513.349	-8.051	-	-	-	-	-
			1538	-39.691	-	-	-	-	-
		0.3	-536.659	-16.033	-	-	-	-	-
			828.873	-4.502	910.074	-6.805	81.721	869.4	1.511

Compound	Conc. (mM)	(V/s)	Epc (mV)	Ipc (μA)	Epa (mV)	Ipa (μA)	ΔE (mV)	$E_{1/2}$ (mV)	$^{ipa}/_{ipc}$
CuANpy	1	0.1	-469.797	-10.91	-	-	-	-	-
			-1491	-38.512	-	-	-	-	-
		0.3	-529.221	-18.023	-	-	-	-	-
			-1440	-40.823	-	-	-	-	-
			-16697	-26.405	-	-	-	-	-
			821.282	-3.404	-	--	-	-	-
CuANbpy	1	0.1	-493.41	-4.35	-	-	-	-	-
			-1293	-24.092	-1392	17.298	99	-1.3425	-0.717
			-1470	-18.854	-1365	26.119	105	1.417	-1.38
		0.3	-523.241	-8.348	-53.054	5.173	-129.813	-588.1475	-0.62
			-1339	-46.267	-	-	-	-	-
			-1477	-18.072	-	-	-	-	-
			-	-	-1347	18.223	-	-	-
CuAN C$_1$VPF$_6^-$	1	0.1	-661.641	-22.83	-	-	-	-	-
			-	-	22.489	-70.619	-	-	-
		0.3	-712.785	-25.14	-	-	-	-	-
			-1140	-9.61	-	-	-	-	-
			-	-	-99.449	31.781	-	-	-
			-	-	685.872	14.645	-	-	-
CuAN V$_2^{2+}$.2PF$_6$-	1	0.1	-377.862	-12.212	-460.560	13.729	82.734	419.229	1.1242
			-637.949	-163.261	-732.721	5.036	-94.77	-685.33	-0.03
			-1283	-107.939	-1302	30.864	-19	-1.29	-0.28
			-1627	-24.351	-	-	-	-	-
			-679.661	-255.036	-	-	-	-	-
		0.3	-1315	-130.82	-	-	-	-	-
			-	-	-1242	55.637	-	-	-
			-	-	-502.091	18.797	-	-	-
			742.075	-34.703	-	-	-	-	-
			-	-	825.423	18.759	-	-	-

Table 4. (*Continued*)

Figures 24, 25 depict the CVs and the potential data are Summarized in **Table 4. Figure 26** present the Cvs at 0.3 and 0.5 V/s by voltage scanning in the positive direction. The irreversible Oxidation peaks observed at 845.666 mV and 938.291 mV at 0.3 and 0.5 V/s are ascribed to the $Cu^{2+}\rightarrow Cu^{1+} + e^-$ Oxidation processes. Typically, this anodic process is Cathodically shifted in CuAN and CuANbpy due to the increase of the electron density at the copper ion upon Complexation (**Table 4**). The higher electron density at the copper ion Corresponds the easier oxidation process (lower Epa) at the copper ion. Therefore, the electron density and hence the easier oxidation process of copper ion ($Cu^{2+}\rightarrow Cu^{1+} + e^-$) increases and follows the order: $Cu(OAC)_2$ < CuAN < CuANpy. The $Cu^{2+}\rightarrow Cu^{1+}$ oxidation processes for $CuANC_1V^+.PF_6^-$ and $CuANV_2^{2+}.2PF_6^-$ are noted at Epa = 685.872 mV and 825.423 respectively. That indicates higher electron density at the Copper ion in $CuANC_1V^+.PF_6^-$ than that in $CuANV_2^{2+}.2PF_6^-$. The more stable Complexes towards oxidation, the higher Epa values. The reduction process: $Cu^{2+} + e^- \rightarrow Cu^{1+}$ occurred at Epc = -377.862 mV, -469.797 mV, -493.413 mV and -513.349 mV for $CuANV_2^{2+}.2PF_6^-$, CuANpy, CuANbpy and CuAN respectively [39,40]. The easier reduction at Cu^{2+} ion means the lower electron density at this ion. Therefore, the easier reduction decreases in the order: $CuANV_2^{2+}.2PF_6^-$, CuANpy, CuANbpy and CuAN which Corresponds the higher electron density at the copper ion following the previous order. The irreversible reduction of the free, N_2O_2 ligand: AN happened at Epc = -1.747 V (at 0.1V/s). This cathodic process was anodically shifted to -1.583 V in the CuAN Complex indicating easier reduction for the Coordinated AN Compared with The free AN, i.e. lower electronic density for the coordinated AN in the Complex CuAN. The CVs of bpy at 0.3 and 0.5 V/s are depicted in **Figure 22**. The nearly quasi-reversible redox Couple was at $E_{1/2}$= 939.7645 mV at 0.5 V/s which is relented with one-electron reduction. The square Pyramidal Complexes: CuANpy and CuANbpy showed two reduction peaks at -1.44V, -1.6697 and -1.339 V, -1.477 respectively [34]. These two reductions peaks are attributed to reductions of coordinated py, AN in CuANpy and Coordinated bpy and AN in CuANbpy respectively. From these redox values, it is clear that the reductions of Coordinated AN. Theoretically, electrochemically reversible one-electron transfer processes are characterized with $\Delta EP = 59$ mV and ipa/ipc ≈ 1. As shown in **Table 4,** the ipa/ipc ration approached 1for the redox wave of the Coordinated bpy in CuANbpy (at 0.3 V/s) but the ΔEP Value was in the range 130-170 mV (130 mV at 0.3V/s) scan rates, which showed a quasi-reversible redox step. The CVs of $C_1V^+.PF_6^-$ at two voltage scan rates (0.3 V/s and 0.5 V/s) are presented in **Figure 27.** One quasi-reversible redox step occurred at $E_{1/2}$ = -970.28 mV (at 0.3 V/s: ΔE =135.44mV, ipa/ipc = 0.9606) which is related to one-electron reduction of $C_1V^+.PF_6^-$ to $C_1V^{\cdot}$ viologen radical. Upon Coordination of $C_1V^+.PF_6^-$ to the Cu^{2+} ion in CuAN $C_1V^+.PF_6^-$ Complex, this reduction process easily happened and ovas anodically shifted to-712.785 mV (at 0.3 V/s) (Compared to that for the free $C_1V^+.PF_6^-$ occurred at -1.038V). This anodic shift is undoubtedly attributed to the formation of the intermolecular dimerization between two $C_1V\cdot$ belonging to two $CuANC_1V^+.PF_6^-$ Complexes. The second cathodic peak noted at -1.14V in CuAN $C_1V^+.PF_6^-$. is attributed to the reduction of the Coordinated AN. In the negative potential scan, one anodic peak at - 70.619 mV is noted that was shifted to -99.449 mV at 0.3V/s. This peak could be Correlated to the anodic peak potention of Cu^{2+} atom. The oxidations of the coordinated Cu^{2+} atom namely: $Cu^{2+} \rightarrow Cu^{3+} + e^-$ and $Cu^{3+} \rightarrow Cu^{4+} + e^-$ are noted at 685.872 mV and 954.853 mV respectively. The first oxidation process (685.872 mV) is easier to happen Compared with that in the salt $Cu(OAC)_2$ (845.666 mV) [41]. This is perfectly Consonant with the higher electron density of the Copper ion in the Complex CuAN $C_1V^+.PF_6$ compared with the case in its origin salt. The reduction of the free ligand AN occurred at -1.747 V has been dropped to -1.583V, -1.491V, - 1.47 V and -1.14V (at 0.3V/s) respectively in the Complexes CuAN, CuANpy, CuANbpy and $CuANC_1V^+.PF_6^-$. This Indicates to the easier reduction and hence higher need to electron density following same previous order. **Figure 27** depicts CVs of $V_2^{2+}.2PF_6^-$, at two voltage Scan rates: 0.1 and 0.5 V/s. During the potential Scan. from o to - 1.2 V, the $V_2^{2+}.2PF_6^-$ shows two Consecutive one-electron reversible CV waves. These waves for $V_2^{2+}.2PF_6^-$ occurred respectively at $E_{1/2}$ = -470.947 mV and -651.444 mV leading to the radical-cation species $V_2^{+\cdot}$ and then to the neutral quinoid Species V^0 respectively. The second redox step is less reversible than the first redox one.

Upon complexation of the terminal nitrogen of the $V_2^{2+}.2PF_6^-$ with Cu^{2+} ion in the complex $CuANV_2^{2+}.2PF_6^-$, two irreversible reduction peaks are noted at Epc= -637.949 mV and E^2pc = -1.283V respectively. Both of these reductions are highly shifted to negative potentials Compared with those of the free $V_2^{2+}.2PF_6^-$ (-504.915mV and -690.779 mV). This shift could be related to the favor intramolecular dimerization among the two viologen radicals within the structure of the Complex. The reversible reduction of Cu^{2+} to Cu^{1+} happened at $E_{1/2}$ = -419.229 mV (at 0.1 V/s). This reduction (Epc= -377.862 mV) is notably easier Compared with that (Epc = -513.349 mV) of the parent complex: CuAN. This anodically shifted Value could be due to the axial positive ligand $V_2^{2+}.2PF_6^-$ in the complex $CuANV_2^{2+}.2PF_6^-$. The oxidation of Cu^{2+} to Cu^{3+} happened at 825.423 mV which was harder than that of $CuANC_1V^+.PF_6^-$.

3.7. Reduction study (formation of molecular switches)

The adduct Complexes (CuANC$_1$V$^+$.PF$_6^-$ and CuANV$_2^{2+}$.2PF$_6^-$) are reduced by activated zinc powder in DMF under argon atmosphere [42]. The UV-Visible absorption spectra are recorded for these resulted reduced solutions and presented in **Figures 28 to 31.** The reduced solutions are oxidized under air atmosphere and their absorption spectra are also presented.

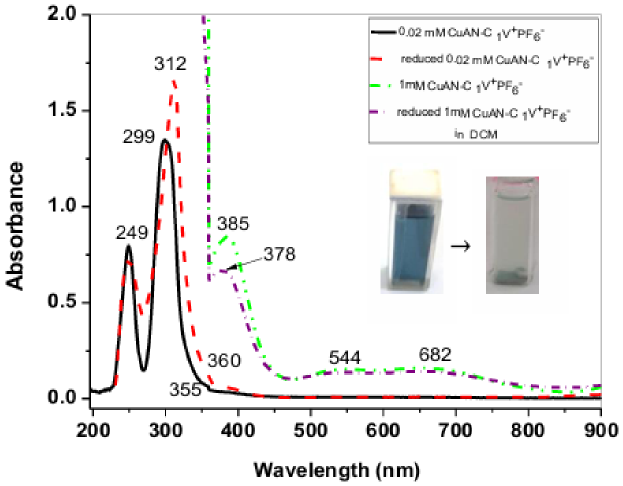

Figure 28. UV-Visible absorption spectra of 0.02 mM (black solid line), 1 mM CuAN-C$_1$V$^+$ PF$_6^-$ (Green dash dot dot) and reduced 0.02 mM (red dash), 1 mM CuAN-C$_1$V$^+$ PF$_6^-$ (purple short dot) in DCM at r.t. using quartz cell with a path length of 1cm.

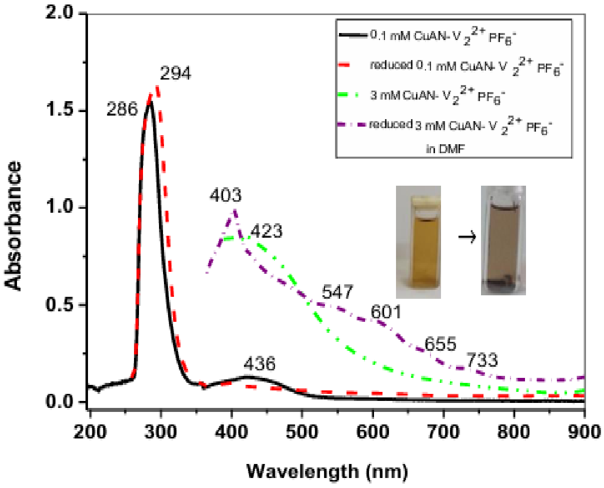

Figure 29. UV-Visible absorption spectra of 0. 1 mM (black solid line), 3mM CuAN-V$_2^{2+}$.2PF$_6^-$ (Green dash dot dot) and reduced 0.1mM (red dash), 3mM CuAN-V$_2^{2+}$.2PF$_6^-$ (purple short dot) in DMF at r.t. using quartz cell with a path length of 1cm.

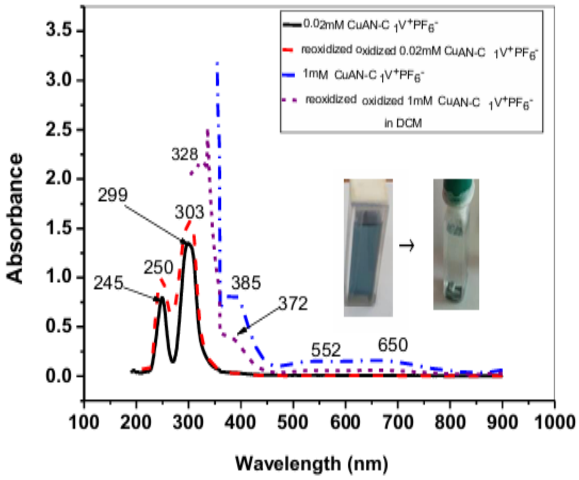

Figure 30. UV-Visible absorption spectra of 0.02 mM (black solid line), 1 mM CuAN-C$_1$V$^+$ PF$_6^-$ (blue dash dot dot) and oxidized 0.02 mM (red dash), 1 mM CuA-C$_1$V$^+$ PF$_6^-$ (purple short dot) in DCM at r.t. using quartz cell with a path length of 1cm.

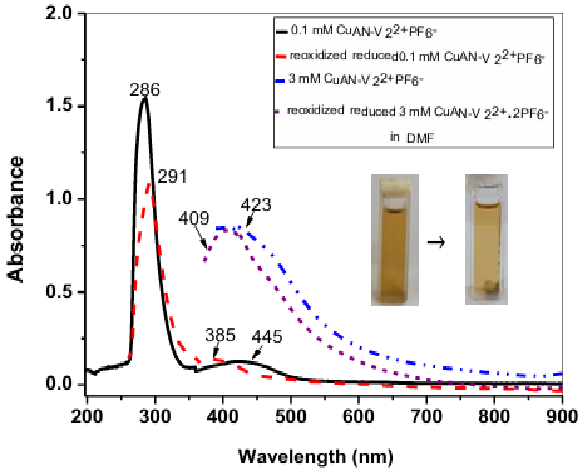

Figure 31. UV-Visible absorption spectra of 0.1 mM (black solid line), 3mM CuAN-V$_2^{2+}$.2PF$_6^-$ (Green dash dot dot) and reduced 0.1 mM (red dash), 3mM CuAN-V$_2^{2+}$.2PF$_6^-$ (purple short dot) in DMF at r.t. using quartz cell with a path length of 1cm.

The absorption Spectra of the reduced CuANV$_2^{2+}$.2PF$_6^-$ (2e-reduced V$_2^{2+}$.2PF$_6^-$ in the complex CuAN-V$_2^{2+}$.2PF$_6^-$) showed UV transition that is red shifted compared with that of oxidized complex. Additionally, the new visible absorptions occurred at 403 nm, 601 nm, 655 nm and 733 nm are attributed to non-dimerized viologen radicals with the Structure of the reduced complex [43-46]. But, the absorption at 547 nm in attributed to the Intermolecularly dimerized viologen radicals in the reduced complex. This corresponds to existence a mixture of non-dimerized viologen radicals and dimerized viologen radicals with structure of the reduced complex as shown in the following **Figure 32.**

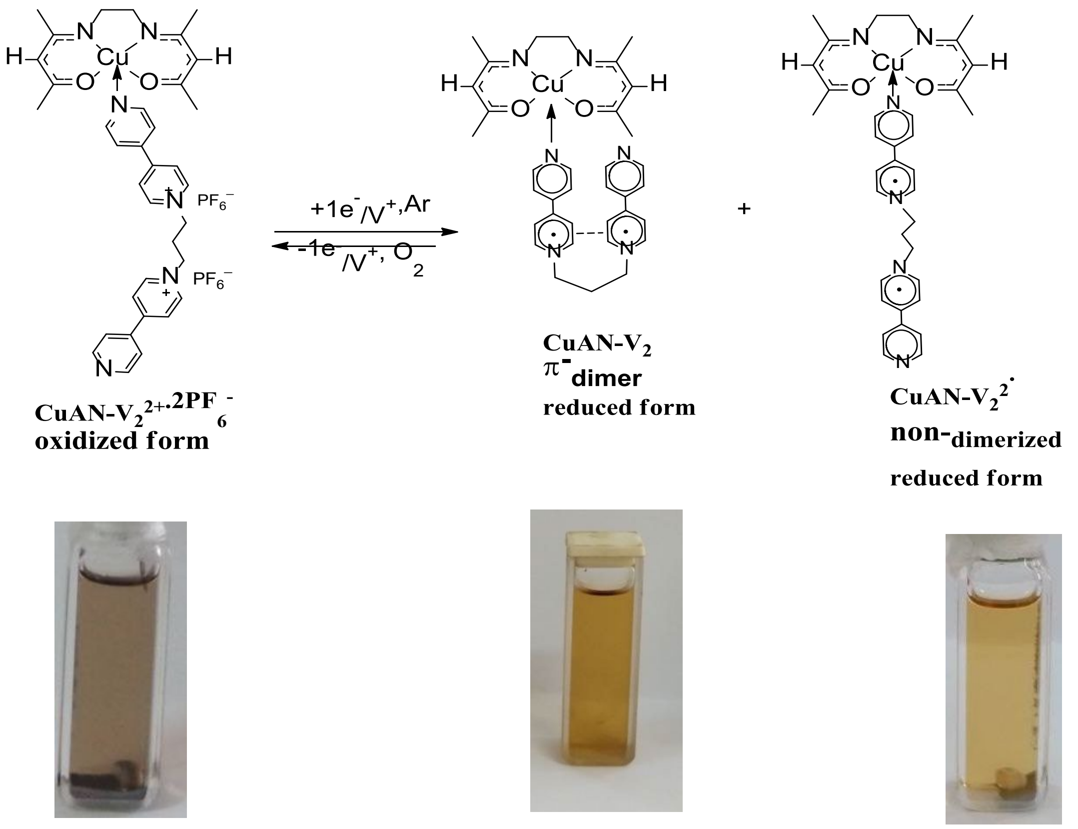

Figure 32. Intermolecular dimerized viologen radicals of (CuAN-V$_2^{2+}$) and non- dimerized viologen radicals (CuAN-V$_2^{2+}$) of CuAN-V$_2^{2+}$.2PF$_6^-$.

Indeed, the existence of oxygen in the solution of reduced complex led to breaking the π-dimer structure and disappearance of the absorptions of dimerized viologen radicals and the red shift of the band 403 nm to 409 nm, Also, a blue shift in UV absorption was noted to be closer to that of the initial oxidized from, see **Figure 33.** Upon reduction of the complex CuANC$_1$V$^+$.PF$_6^-$, usual red shift in UV absorption are noted compared with those of the oxidized Complex (245 nm to 249 nm and 299 nm to 312 nm) [47]. Additionally, the visible absorptions of the oxidized complex: 385 nm, 552 nm and 650 nm are blue shifted to 378 nm, blue shifted to 544 nm and red shifted to 682 nm. These absorption Changes are due to the formation of π-dimerization between two viologen radicals belonging to two complex molecules, see the following **Figure 33.**

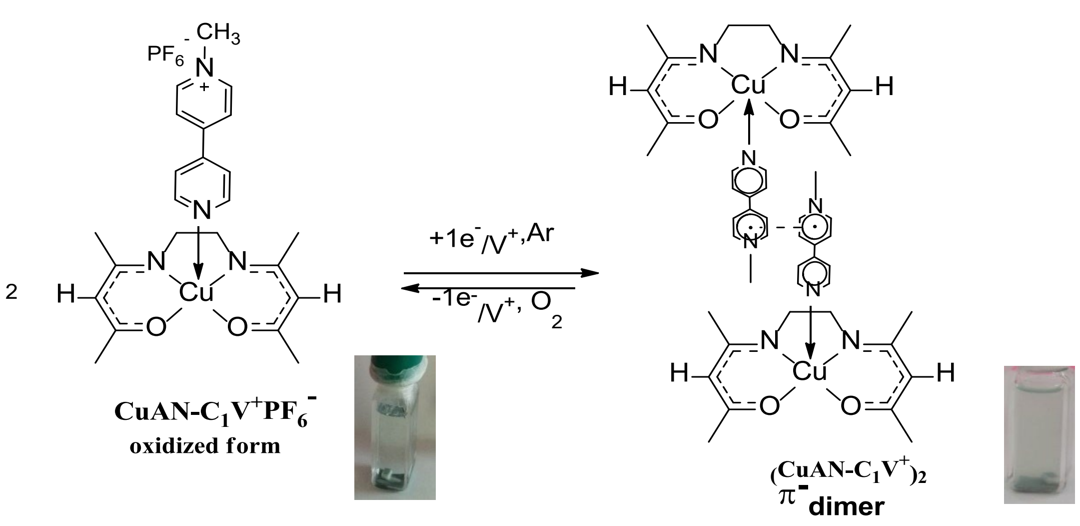

Figure 33. Intermolecular dimerized viologen radicals of CuANC$_1$V$^+$.PF$_6^-$, (CuANC$_1$V$^+$)$_2$.

4. Conclusion

The reaction of the copper (II) bis(acetylacetonato) ethylenediimine (CuAN) with Pyridine, mono-methylviologen ($C_1V^+.PF_6^-$) and bis-viologen ($V_2^{2+}.2PF_6^-$**)** at lab temperature yielded the adduct complexes CuAN-py, CuAN-$C_1V^+.PF_6^-$ and CuAN$V_2{}^{2+}.2PF_6^-$ respectively are characterized them by mass, FT-IR, UV-Visible absorption spectrometry, XRD diffraction, thermal analyses and Cyclic voltammetry. The mass spectroscopy confirmed the complexes structures through the appearance of the molecular ion, the dimer of the molecular ion or a fragment from the molecular ion and the mass fragmentations are also suggested. EDS spectroscopy showed the elements peaks and the SEM explained the dramatic differences among complexes in terms of particle shape, particle size, surface texture, particle distribution etc. UV transitions of ligand and complex besides the d-d transitions of complexes are compared, elucidated and connected appropriately with structures. The XRD spectra of the complexes showed that with ligand and complex are crystalline. The d-spacing values have been calculated, discussed and connected to complex and ligand structure. The SEM results confirmed XRD findings. The TG-DTA for ligand and complexes have showed that the thermal stability increases in the sequence: CuANpy< CuAbpy < CuAN< CuANbpy < CuAN$V_2^{2+}.2PF_6^-$. The viologen units complexed to copper (II) ion within the novel copper complexes are deduced by chemical and electrochemical stimuli. The switching movements among viologen radicals and viologen π-dimers are proved by cyclic voltammetry and UV-visible absorption spectroscopy. Overall, the study highlights the new pathway for developing Cu(II)-viologen complexes with axial coordination and reversible π–dimerization.

Acknowledgements

The author would like to express sincere gratitude to Dr. Wathiq Sattar for his valuable guidance, continuous support, and insightful advice throughout the research period. His expertise and encouragement played a key role in the successful completion of this work.

Conflict of interest

The authors declare no conflict of interest

References

1. Saladino R; Chidichimo G; Versace C. Study of innovative electrochromic films 2009.
2. De Benedittis M; De Simone BC; Longeri M. Solar control solid organic electrochromic films 2006.
3. Kathiresan M; Ambrose B; Angulakshmi N; Mathew DE; Sujatha D; Stephan AM. Viologens: a versatile organic molecule for energy storage applications. Journal of Materials Chemistry A. 2021;9(48):27215-27233
4. Striepe L; Baumgartner T. Viologens and their application as functional materials. Chemistry–A European Journal. 2017;23(67):16924-16940
5. Li X; Yang J; Yang Y-W. Recent advances of stimuli-responsive viologen-based nanocomposites. Materials Chemistry Frontiers. 2023;7(8):1463-1481
6. Škorjanc T; Shetty D; Olson MA; Trabolsi A. Design strategies and redox-dependent applications of insoluble viologen-based covalent organic polymers. ACS applied materials & interfaces. 2019;11(7):6705-6716
7. Gogoi K; Chakraborty S. Impact on Redox Characteristics of Rotaxane via Structural Modifications. ChemistrySelect. 2025;10(17):e202501216
8. Smith ES; Lilienthal RR; Fonseca RJ; Smith DK. Electrochemical characterization of a viologen-based redox-dependent receptor for neutral organic molecules. Analytical Chemistry. 1994;66(19):3013-3020
9. Sagara T; Tahara H. Redox of viologen for powering and coloring. The Chemical Record. 2021;21(9):2375-2388
10. Mihsen HH. Synthesis, Characterization, and Biological Activitiy of Copper (II) Complexes Containing Bidentate Schiff Bases. University of Thi-Qar Journal of Science. 2014;4(2):59-65
11. Bis-viologen PS. Archive of SID. ir. 2023
12. Abdul WS; Musaa AM. Iron (II), cobalt (II), and nickel (II) complexes of bis-(3-chloroacetylacetonate) ethylenediimine and bis-(acetylacetonate) ethylenediimine and their viologen molecular switches.
13. Xue Z; Daran J-C; Champouret Y; Poli R. Ligand adducts of bis (acetylacetonato) iron (II): a 1H NMR study. Inorganic Chemistry. 2011;50(22):11543-11551
14. Jassema IA; Abdul-Hassana WS; Flafela IA; Jghebilb HO. Axial ligation for copper (II) complexes of bis (acetylacetonato) ethylenediimine and bis (3-chloroacetylacetonato) ethylenediimine. 2023

15. SINGH R; NEERUPAMA GK; SHARMA P; SACHAR R. Synthesis, Characterization and Antifungal Activity of Adducts of Bis (acetylacetonato) oxovanadium (IV) with Heterocyclic Nitrogen Donor Ligands. Chemical Science. 2014;3(3):1099-1109
16. Santana-Marques MGO; Amado FM; Correia AF; Lucena M; Madureira J; Goodfellow BJ; Félix V; Santos TM. Characterization and differentiation of ruthenium (II) complexes with 1, 4, 7-trithiacyclononane and nitrogen heterocycles by electrospray mass spectrometry. Journal of mass spectrometry. 2001;36(5):529-537
17. Thejeel E; Mekky AH. Synthesis, Absorption, Distribution, Metabolism, Excretion, Toxicology (ADMET) and molecular docking studies of some pyridin-2 (1H)-one derived from a Apocynin in Thi-Qar Governorate. University of Thi-Qar Journal of Science. 2023;10(2):73-80
18. Zhao L; Song X; Gong C; Zhang D; Wang R; Zare RN; Zhang X. Sprayed water microdroplets containing dissolved pyridine spontaneously generate pyridyl anions. Proceedings of the National Academy of Sciences. 2022;119(12):e2200991119
19. Kaya B; Akyüz D; Karakurt T; Şahin O; Koca A; Ülküseven B. Cobalt (II)/(III) complexes bearing a tetradentate thiosemicarbazone: Synthesis, experimental and theoretical characterization, and electrochemical and antioxidant properties. Applied Organometallic Chemistry. 2020;34(11):e5930
20. Mekky AH; Dalal MJ; Sager AG; Salmn NAA; Abd Ali AT; Jayapal M. Synthesis, characterization and Theoretical study of some 2-Oxopyridine Carbonitrile derivatives that contain tetrazole ring and evaluation of their Biological activity. University of Thi-Qar Journal of Science. 2023;10(2):235-241
21. Batool M; Haider MN; Javed T. Applications of spectroscopic techniques for characterization of polymer nanocomposite: A review. Journal of Inorganic and Organometallic Polymers and Materials. 2022;32(12):4478-4503
22. Chen Y-Y; Chu DE; McKinney BD; Willis LJ; Cummings SC. High-spin, five-coordinate complexes of cobalt (II), nickel (II), and copper (II) with linear, pentadentate keto, iminato ligands. Inorganic Chemistry. 1981;20(6):1885-1892
23. Krisyuk VV; Baidina IA; Romanenko GV; Kryuchkova NA; Shayapov VR; Komarov VY; Kyzy SU; Benassi E; Igumenov IK. Structural Diversity and Spectral Properties of the Crystals of Heterometallic Complexes Derived from TM (acacen) and Pb (diketonate) 2, TM= Cu, Ni, Pd. Crystal Growth & Design. 2020;20(11):7260-7270
24. Kumar A; Kurbah SD; Syiemlieh I; Dhanpat SA; Borthakur R; Lal RA. Synthesis, characterization, reactivity, and catalytic studies of heterobimetallic vanadium (V) complexes containing hydrazone ligands. Inorganica Chimica Acta. 2021;515:120068
25. Maurya MR; Khurana S; Zhang W; Rehder D. Biomimetic oxo-, dioxo-and oxo-peroxo-hydrazonato-vanadium (IV/V) complexes. Journal of the Chemical Society, Dalton Transactions. 2002(15):3015-3023
26. Poralan G; Gambe J; Alcantara E; Vequizo R, editors. X-ray diffraction and infrared spectroscopy analyses on the crystallinity of engineered biological hydroxyapatite for medical application. IOP conference series: materials science and engineering; 2015: IOP Publishing.
27. Lalancette RA; Syzdek D; Grebowicz J; Arslan E; Bernal I. The thermal decomposition and analyses of metal tris-acetylacetonates: Free radical formation from Al, Cr, Mn, Fe and Co complexes. Journal of Thermal Analysis and Calorimetry. 2019;135(6):3463-3470
28. Al-Dobony BS; Al-Assafe AY, editors. Synthesis, characterization and antimicrobial studies of some metal complexes with mixed ligands derived from Mannich bases and diamine ligands. Journal of Physics: Conference Series; 2019: IOP Publishing.
29. Farrukh MA; Butt KM; Chong K-K; Chang WS. Photoluminescence emission behavior on the reduced band gap of Fe doping in CeO2-SiO2 nanocomposite and photophysical properties. Journal of Saudi Chemical Society. 2019;23(5):561-575
30. Kurzak B; Kamecka A; Bogusz K; Jezierska J. Stabilities and coordination modes of histidine in copper (II) mixed-ligand complexes with ethylenediamine, diethylenetriamine or N, N, N′, N ″, N ″-pentamethyldiethylenetriamine in aqueous solution. Polyhedron. 2008;27(13):2952-2958
31. Bols ML; Ma J; Rammal F; Plessers D; Wu X; Navarro-Jaén S; Heyer AJ; Sels BF; Solomon EI; Schoonheydt RA. In situ UV–Vis–NIR absorption spectroscopy and catalysis. Chemical reviews. 2024;124(5):2352-2418
32. Brzezinski B; Zundel G. Influence of solvents on intramolecular hydrogen bonds with large proton polarizability. Journal of Magnetic Resonance (1969). 1982;48(3):361-366
33. Kianfara A; Zargari S; Khavasi H. Synthesis and electrochemistry of M (II) N2O2 schiff base complexes: X-Ray structure of {Ni [Bis (3-chloroacetylacetone) ethylenediimine]}. Journal of the Iranian Chemical Society. 2010;7(4):908-916
34. Balewski Ł; Inkielewicz-Stępniak I; Gdaniec M; Turecka K; Hering A; Ordyszewska A; Kornicka A. Synthesis, structure, and stability of copper (II) complexes containing imidazoline-phthalazine ligands with potential anticancer activity. Pharmaceuticals. 2025;18(3):375
35. Conradie MM. Cu (β-diketonato) 2 bathochromic shifts from the ultraviolet towards the visible region. Journal of Molecular Modeling. 2024;30(10):336
36. Zhou M; Song L; Niu F; Shu K; Chai W. A square-pyramidal copper (II) complex with strong intramolecular hydrogen bonds: diaqua (N, N′-dimethylformamide-κO) bis [2-(diphenylphosphoryl) benzoato-κO] copper (II). Crystal Structure Communications. 2013;69(5):463-466

37. Eshaghi Malekshah R; Salehi M; Kubicki M; Khaleghian A. New mononuclear copper (II) complexes from β-diketone and β-keto ester N-donor heterocyclic ligands: structure, bioactivity, and molecular simulation studies. Journal of Coordination Chemistry. 2018;71(7):952-968
38. Al-Harazie AG; Gomaa EA; Zaky RR; Abd El-Hady MN. Spectroscopic characterization, cyclic voltammetry, biological investigations, MOE, and gaussian calculations of VO (II), Cu (II), and Cd (II) heteroleptic complexes. ACS omega. 2023;8(15):13605-13625
39. Yamada H; Yoshii K; Asahi M; Chiku M; Kitazumi Y. Cyclic voltammetry part 1: fundamentals. Electrochemistry. 2022;90(10):102005-102005
40. Elgrishi N; Rountree KJ; McCarthy BD; Rountree ES; Eisenhart TT; Dempsey JL. A practical beginner's guide to cyclic voltammetry. Journal of chemical education. 2018;95(2):197-206
41. Soofivand F; Salavati-Niasari M. Novel solvent-less synthesis of CuO nanoparticles by using sublimated precursors. Materials Letters. 2013;106:83-86
42. Sharma M; Tripathi J; Yadav A; Jha S; Mishra A; Shrivastava B, editors. Structural characterizations of copper complex using x-ray diffraction and x-ray absorption fine structure spectroscopy. AIP Conference Proceedings; 2019: AIP Publishing LLC.
43. Bangi UK; Lee K-Y; Maldar NMN; Park H-H. Synthesis and properties of metal oxide aerogels via ambient pressure drying. Journal of nanoscience and nanotechnology. 2019;19(3):1217-1227
44. He K; Chen N; Wang C; Wei L; Chen J. Method for determining crystal grain size by x-ray diffraction. Crystal Research and Technology. 2018;53(2):1700157
45. Warren B; Averbach B. The separation of cold-work distortion and particle size broadening in X-ray patterns. Journal of applied physics. 1952;23(NYO-765)
46. Rabiei M; Palevicius A; Monshi A; Nasiri S; Vilkauskas A; Janusas G. Comparing methods for calculating nano crystal size of natural hydroxyapatite using X-ray diffraction. Nanomaterials. 2020;10(9):1627
47. Qian Y; Yang H; Wang Y. A novel bis (terpyridine) with π− conjugated phenyl viologen and its metallo-supramolecular polymers: Synthesis and electrochromism. Dyes and Pigments. 2020;176:108251
48. Karim AN, Jasim LS. Synthesis and characterization of poly (CH/AA-co-AM) composite: Adsorption and thermodynamic studies of benzocaine on from aqueous solutions. International Journal of Drug Delivery Technology. 2019;9(4):558-62
49. AlSaadi EK, Darweesh MA, Al Jawadi HF, Othman MAM. Demographic Characteristics, Clinical Features, Laboratory, and Radiological Findings in Children Admitted to COVID19 Center in Amara City, Misan Province, Iraq. Journal of Medicinal and Chemical Sciences. 2023;6(1):34-43.
50. Al-Suraify SMT. Synthesis and characterization of new heterocyclic compounds in corporating heterocyclic moiety derived from 3-chloro-1-methyl-1h-indazole. Biochemical and Cellular Archives. 2020;20:4127-34.
51. Al-Suraify SMT, Mekky AH, Husssien LB. Synthesis of new nitrogenous derivatives based on 3-chloro–1-methyl-1H-indazole. International Journal of Pharmaceutical Research. 2020;12:793-802.